ISRN LUTMDN/TMHP-21/5461-SE

ISSN 0282-1990

LUNDS UNIVERSITET

The Investigation and Modeling of Paperboard Clippings in a Pipe Flow

Lea Christierson

Master Thesis degree of Master of Science in Engineering
Division of Fluid Mechanics
Department of Energy Sciences
Faculty of Engineering | Lunds Universitet

The Investigation and Modeling of the interaction between Paperboard Clippings in a Pipe Flow

by Lea Christierson

LUND
UNIVERSITY

This degree project for the degree of Master of Science in Engineering has been conducted at the Division of Fluid Mechanics, Department of Energy Sciences, Faculty of Engineering, Lund University and at Tetra Pak AB in Lund.

The supervisor at Tetra Pak AB was Aurélia Vallier. The supervisor at the Division of Fluid Mechanics was associate senior lecturer Hesameddin Fatehi and the examiner at Lund University was Robert-Zoltán Szász.

Thesis for the Degree of Master of Science in Engineering

ISRN LUTMDN/TMHP-21/5461-SE
ISSN 0282-1990

Division of Fluid Mechanics
Department for Energy Sciences
Faculty of Engineering, Lunds University
Box 118, 221 00 Lund
Sweden

www.energy.lth.se

Abstract

In the manufacturing process of Tetra Pak® packages, holes are cut out of the paperboard for straws and caps. The left-over paperboard clippings, called *confetti*, need to be evacuated from the machine. However, this evacuation process has proven to cause problems due to jams arising as the confetti get stuck in joints and along the pipe walls. This study investigates how the confetti behave, deform and interact with each other, the flow and the pipe walls, to get a better understanding of how and why these jams occur.

Fluid structure interaction (FSI), which is a class of multi-physics and deals with the interaction between fluid flow and deformable structures, is employed to model the confetti in a pipe flow. An FSI-simulation model is developed, by using the software STAR-CCM+ and Abaqus/Standard, and is validated against experimental data.

It is found that the confetti mainly lose kinetic energy, thus evacuation speed, when facing the flow with a small cross-sectional area or getting too close to the pipe wall, decelerating due to the near wall, low velocity flow. Colliding with other confetti or the wall does not affect the evacuation speed negatively. However, the initial position of the confetti influences its initial movement, thus the evacuation speed. A negative initial angle is found to be preferable compared to a positive inclination angle, since this decreases the risk for the confetti getting stuck in the near wall, low velocity flow.

The FSI-simulations coincide well with the experiments, capturing the trajectory of the confetti through the pipe adequately. The simulation model over-predicts the evacuation speed, indicating that some of the losses arising in the experiments are not fully captured by the model. However, the model is considered to capture the course of events to a satisfying extent and can be used for future research and development at Tetra Pak®.

Keywords: Fluid-structure interaction, paperboard material modeling, transient pipe flow, overset mesh, image analysis

Acknowledgments

I would like to begin to thank my supervisors Aurélia Vallier and Hesameddin Fatehi for their constant support, help and encouragement. Aurélia, your never-ending commitment has played such an important role through all steps in this thesis and I have learned so much from you, both within the field of FSI but also on a personal level. Hesam, for motivating me and contributing with so much knowledge within CFD while keeping me in line with the university's requirements, thank you.

My colleagues at Tetra Pak® deserve to be acknowledged. Despite the pandemic prompted home office for the main part of the thesis, you were always open for questions and a weekly online-fika. I would like to especially acknowledge the help I got from Gustaf for participating in weekly meetings and for his invaluable input. To Eskil, Andreas and Johan, for helping me getting started with Abaqus and debugging non-compliant simulations. Furthermore, I wish to thank Magnus, Niklas and Bengt who helped me with the lab equipment and the high-speed camera, making the physical experiments possible. Mani, from STAR-CCM+, deserves huge acknowledgment for helping me setting up this new kind of FSI-simulation case. It has been a real pleasure to work with you all.

Finally, I would like to thank my family and friends for your unwavering support and encouragement. Without you, this would not have been possible.

Lea Christierson
Lund, January 2021

Contents

List of Figures

List of Tables

Nomenclature

Roman letters

a	Acceleration
$\mathbf{a}$	Nodal displacement matrix
b	Body force
$\mathbf{c}$	Arbitrary column vector
$\mathbb{C}$	Compliance tensor
$\mathbf{D}$	Stiffness tensor
$\mathbb{D}^{ep}$	Elasto-plastic stiffness tensor
D	Diameter
E	Total energy, in Section 3
E	Young's modulus, in Section 2
F	Force
f	Yield function
f_{ext}	External force
f_{int}	Internal force
G	Shear moduli
H	Plastic modulus
K	Hardening parameter
k	Conductivity, in Section 3
k	Turbulent kinetic energy, in Section 3
k	Constant for pressure-overclosure relation, in Section 2
m	Mass
$\mathbf{M}$	Mass matrix
$\mathbf{N}$	Global shape function matrix
p	Pressure
R	Ideal gas constant
R_{ij}	Anisotropic yield stress ratio
$\mathbf{s}$	Deviatoric stress
S	Mean strain rate of deformation matrix, in Section 3
S	Surface, in Section 2
$\mathbf{S_E}$	Source term for potential energy
$\mathbf{S_M}$	Source term for body forces
t	Time, in Section 3
t	Traction force, in Section 2
T	Temperature
$\mathbf{u}$	Velocity vector, in Section 3
u	Displacement, in Section 2
u	x-component of velocity, in Section 3
$\ddot{u}$	Acceleration, second time derivative of u, in Section 2
u_t	Friction velocity
v	y-component of velocity, in Section 3
v_i	Weight function
V	Volume
w	z-component of velocity, in Section 3

Greek letters

ϵ	Total strain, in Section 2
ϵ	Dissipation rate of turbulent kinetic energy, in Section 3

ϵ^e	Elastic strain, in Section 2
ϵ^p	Plastic strain, in Section 2
ϵ^p_{eff}	Effective plastic strain, in Section 2
κ	Internal state variables
λ	Plastic multiplier
μ	Dynamic viscosity
μ_t	Turbulent viscosity
ν	Kinematic viscosity, in Section 3
ν	Poisson's ratio, in Section 2
ρ	Density
σ	Stress
σ_y	(Current) yield stress
σ_{y0}	Initial yield stress
$\boldsymbol{\tau}$	Viscous stress tensor
τ_w	Wall shear stress

Abbreviations

CD	Cross-machine direction
CFD	Computational fluid dynamics
FEM	Finite element method
FSI	Fluid-structure interaction
MD	Machine direction
RANS	Reynolds averaged Navier-Stokes
RBF	Radial basis function
Re	Reynolds number
ZD	Out-of-plane direction

Chapter 1

Introduction

In the pursuit of constantly increasing performance and optimizing products, most larger companies see the importance of research and development. With an ever-increasing availability and size of computational resources at the disposal to engineers and researchers, multi-physics simulations are becoming more present than ever before. Especially, fluid-structure interaction (FSI), a class of multi-physics problems, has gained much attention. Modeling the interaction between fluids and deformable structures, FSI finds application in the broadest range of fields. Solving problems within engineering, life science, aerodynamics and modeling blood flow through vessels, it is a powerful tool for solving complex problems. [1]

1.1 Background

Tetra Pak® is a company that supplies complete systems for processing, packaging and distribution of liquid food and beverages. The packaging material is manufactured in converting factories. A roll with paperboard enters the converting machine where it is printed with the correct print design, fold creases are prepared, and holes for straws or screw caps are cut out. Afterwards, the paperboard is laminated with plastic and aluminum foil to create a dense and strong packaging material and is rolled onto smaller rolls for delivery to the packaging machine. In the packaging machine, the packaging material is folded into packages along the prepared folding creases, sterilized, filled with liquid food or beverages and finally sealed off, as depicted in Fig. 1.1. The finished product exits the machine, ready to be distributed. [2]

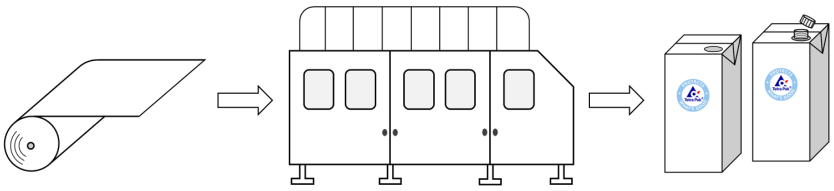

Figure 1.1: A conceptual sketch of a packaging machine.

As the holes are cut out of the paperboard, small paperboard discs are produced as waste. These paperboard discs are the subject of interest in this project. They are called *confetti* and can have different shapes, depending on the package shape and volume and what

it will contain, as shown in Fig. 1.2. Since the confetti are not a part of the final package, they must be removed from the converting machine through a confetti evacuation system.

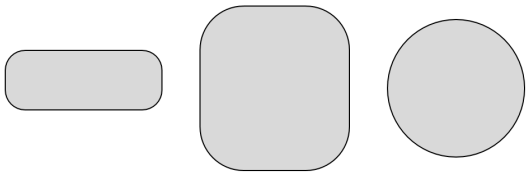

Figure 1.2: The most common confetti shapes that occur; rectangular, square and round.

The holes are cut out of the paperboard by knives, placed in one of the rollers in the cutting unit of the converting machine through which the paperboard is fed, as shown in Fig. 1.3a. As the holes are cut, the confetti that is formed is sucked into the roller via tubes. These tubes connect the knife at the surface of the roller to a central main pipe, that runs coaxial in the roller, Fig. 1.3b. Fans are connected to the main pipe, to suck the confetti out, thus the confetti is removed from the main pipe and ultimately from the converting machine.

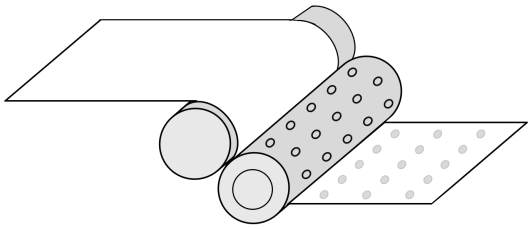

(a) Rollers through which a sheet of paperboard is fed, where the lower one is equipped with knives.

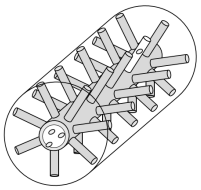

(b) Transparent view of the lower roller, showing the knives, from which the confetti are to be removed.

Figure 1.3: A sketch of the geometry of the system.

It was observed that the confetti tend to get stuck in gaps and joints, and sediment to the wall of the main pipe. Problems with confetti entering one knife and exiting through the opposite one also occurs. Fig. 1.4 displays these problematic behaviors of the confetti that are observed.

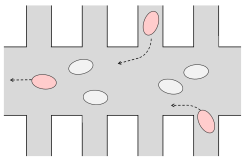

(a) Normal flow

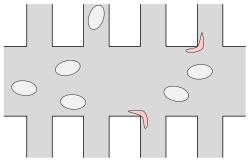

(b) Sticking to joints

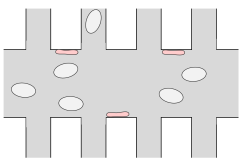

(c) Sticking to wall

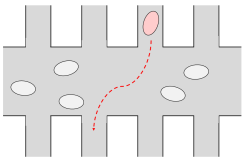

(d) Exiting through opposite knife

Figure 1.4: Illustrations of the different kinds of problems observed when evacuating confetti from the main pipe.

Previously, different variations of the geometry of the knife roller has been investigated. However, the deformation of and the interaction between the confetti as they are evacuated and how they affect the airflow inside the roller has not been studied. As a starting

point, Tetra Pak® created a simple FSI-model of one confetti flying through a straight pipe, in order to fully catch the behavior and deformation of the confetti in a correct way. It is this numerical model that this project is based upon, and is therefore referred to as the *Pre-existing model*, pictured in Fig. 1.5a. The aim of this project is to enhance this Pre-existing model to the domain pictured in Fig. 1.5b, including two confetti and capturing their behavior, deformation and interaction. This will provide a base for future development of the model to include the entire geometry, pictured in Fig. 1.5c, and including several confetti. This would enable a more realistic simulation of what happens inside the knife roller and give insight on how the confetti behave and interact with each other. Since it is not possible to film the course of events inside the machine, this could provide insight on how and why the jams occur. However, due to time limitations, this part of the development is beyond the scope of this project.

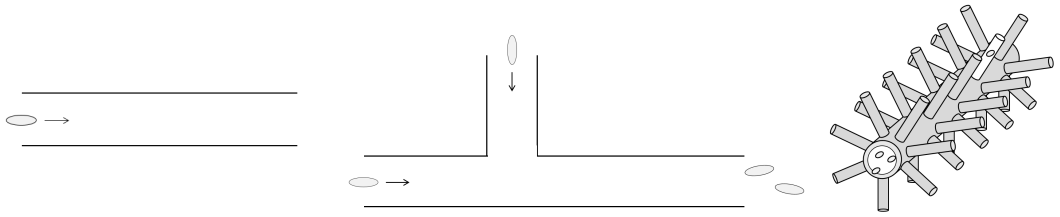

(a) Pre-existing model (b) Model of this project (c) Goal geometry

Figure 1.5: An illustration of the domain that is going to be evaluated in this project.

1.2 Project motivation

This unstable confetti evacuation is of interest for Tetra Pak® since it causes the performance to drop during production. Reducing the number of occasions when these problems arise, or preventing it completely, would entail longer run times for the machines and with it a larger production capacity and a more robust manufacturing process of the packaging material.

To date there is no complete simulation model for this process; where several confetti are being evacuated and that includes the deformation and interaction between the confetti. In this Master Thesis the previously developed model from Tetra Pak®, is to be expanded to include a geometry closer to reality and to include two confetti, to give insight on how the confetti behave, deform and interact in the pipe flow. The challenge lies in the deformation of and the interaction between two confetti and achieving a set-up that models this interaction realistically, that is numerically stable and computational efficient, to capture the course of events accurately.

1.3 Objective

The goal is to develop an FSI-model that can describe the interaction between two confetti and how this interaction causes deformations and affects the displacements of the confetti. Further, this model should be numerically stable to simulate the complete course of events, i.e. the two confetti entering, colliding, interacting and finally exiting the pipe.

The goal is also to complement the simulations with physical experiments to obtain experimental data to validate the results obtained from the numerical model. The results will be compared using image analysis.

1.4 Limitations

To be able to finish this project within the time frame at hand, some limitations had to be made. It was chosen to only look at two confetti simultaneously, at most and the final geometry was limited to a T-junction pipe. These limitations made it possible to make physical experiments to verify and validate the numerical simulations and use an image analysis program to analyze the results from the physical experiments.

Within the project, it was chosen to only analyze one kind of confetti shape, namely the rectangular one. Since it is easy to change the shape of the confetti in the simulation model, this is not as important as the physics and numerics in the FSI-model. Once the model works, Tetra Pak® can change the shape to make further analyses on other confetti shapes.

1.5 Outline of report

In this thesis, relevant theory will first be covered. Sections 2 and 3 give an outline of the solid and fluid mechanics used in an FSI-problem, to give the reader a fundamental understanding of the physics applied in this project. Numerical aspects, such as how the governing equations are solved numerically, are also highlighted. Secondly, the previous work done within this application will be introduced in Section 4, followed by Section 5 explaining how the previous work is used to further develop a model to simulate several confetti in a T-junction pipe. The experimental set-up employed to validate the simulation results, is also covered here, and followed by the results and discussion in Section 6. Here, the results are assessed, and the numerical and experimental results are compared. Lastly, in Section 7, the conclusion are presented and the paper is closed by future research and development.

Chapter 2

Solid Mechanics

The Finite Element Method (FEM) is a commonly used method for solving problems within structural analysis and is a numerical method for solving partial differential equations. The approach used to solve these kinds of problems is to subdivide a large system into smaller, simpler parts called finite elements, which is achieved by using a space discretization implemented by a mesh. The equations that model these finite elements are then assembled into a larger system of equations that models the entire problem.

In this section, the FE-formulation for a structural analysis will be derived and the constitutive material model for paperboard will be explained.

2.1 FE-formulation

The Finite Element formulation provides a discretized approximation of the equation of motion for a solid body. For a comprehensive treatment of the FE-formulation the reader is referred to [3], from which the theory described in this chapter is derived.

The FE-formulation is derived by integrating the equation of motion, Newtons second law, over the body.

$$F = ma \quad \Rightarrow \quad \int_S t_i \, \mathrm{dS} + \int_V b_i \, \mathrm{dV} = \int_V \rho \ddot{u}_i \, \mathrm{dV}$$

Here, the total force, F, is split into a traction (surface) force, t_i, acting on a body with the surface S and a body force, b_i, acting on the body volume denoted by V. The acceleration, defined as the second time derivative of the displacement u, is denoted $\ddot{u}$, ρ is the density and the index $i = x, y, z$ denotes the component of the vector in the respective coordinate system. Rewriting the traction vector as $t_i = \sigma_{ij} n_j$, where σ_{ij} is the stress, n_j is the normal to the surface and the index $j = x, y, z$, and using the divergence theorem, the volume integral can be omitted and the strong form of the problem is obtained, Eq. 2.1.

$$\int_V \frac{\partial \sigma_{ij}}{\partial x_j} \, \mathrm{dV} + \int_V b_i \, \mathrm{dV} = \int_V \rho \ddot{u}_i \, \mathrm{dV} \quad \Rightarrow \quad \frac{\partial \sigma_{ij}}{\partial x_j} + b_i \, \mathrm{dV} = \rho \ddot{u}_i \tag{2.1}$$

Multiplying the strong form with an arbitrary weight function, v_i, and integrating over the body volume V once again, the following equation is obtained.

$$\int_V v_i \frac{\partial \sigma_{ij}}{\partial x_j} \, \mathrm{dV} + \int_V v_i b_i \, \mathrm{dV} = \int_V v_i \rho \ddot{u}_i \, \mathrm{dV} \tag{2.2}$$

Using partial integration and the divergence theorem, the first term in Eq. 2.2 can be rewritten as

$$\int_V v_i \frac{\partial \sigma_{ij}}{\partial x_j} \, \mathrm{dV} = \int_v \frac{\partial (v_i \sigma_{ij})}{\partial x_j} - \int_V \frac{\partial v_i}{\partial x_j} \sigma_{ij} \, \mathrm{dV} = \int_S v_i t_i \, \mathrm{dS} - \int_V \frac{\partial v_i}{\partial x_j} \sigma_{ij} \, \mathrm{dV} \tag{2.3}$$

Here, the partial derivative of the weight function in Eq. 2.3 can be expressed, using the strains, as follows

$$\frac{\partial v_i}{\partial x_j} = \frac{1}{2} \left(\frac{\partial v_i}{\partial x_j} + \frac{\partial v_j}{\partial x_i} \right) + \frac{1}{2} \left(\frac{\partial v_i}{\partial x_j} - \frac{\partial v_j}{\partial x_i} \right) = \epsilon_{ij}^v + 0 \tag{2.4}$$

Inserting Eq. 2.4 into 2.3, and inserting the result into the first term of Eq. 2.2, the final expression for the weak form is obtained as stated in Eq. 2.5 below.

$$\int_V v_i \rho \ddot{u}_i \, \mathrm{dV} + \int_V \epsilon_{ij}^v \sigma_{ij} \, \mathrm{dV} = \int_S v_i t_i \, \mathrm{dS} + \int_V v_i b_i \, \mathrm{dV} \tag{2.5}$$

Eq. 2.5 gives the weak formulation of the equations of motion, which is needed to discretize the equation, i.e. derive the complete FE-formulation in matrix notation.

Using the approximation $\mathbf{u} = \mathbf{N}\mathbf{a} \Rightarrow \ddot{\mathbf{u}} = \mathbf{N}\ddot{\mathbf{a}}$ where $\mathbf{u}$ gives the global displacements, $\mathbf{N}$ are the global shape functions and $\mathbf{a}$ are the nodal displacements, the finite element formulation can be determined. The double dot-notation denotes a second time derivative. The kinematics relation, defined in Eq. 2.6, is used to derive the FE-formulation. It gives a relation for the strains and displacements in matrix-notation and is employed to choose a weight function.

$$\boldsymbol{\epsilon} = \tilde{\nabla} \mathbf{u} \tag{2.6}$$

Here, $\tilde{\nabla}$ represents a matrix differential operator. To derive the FE-formulation, a weight function is needed. For this purpose, the Galerkin method is chosen since it is efficient, and when combined with the weak form, it gives symmetric coefficient matrices which is of advantage in numerical calculations. In the Galerkin method the weight function is chosen, such that it is similar to the global displacements, which gives

$$v = \mathbf{N}\mathbf{c} \quad \Rightarrow \quad \boldsymbol{\epsilon}^v = \tilde{\nabla}\mathbf{N}\mathbf{c} = \mathbf{B}\mathbf{c}, \quad \text{where} \quad \mathbf{B} = \tilde{\nabla}\mathbf{N} \tag{2.7}$$

where $\mathbf{c}$ is an arbitrary column vector. Inserting the formulations from Eq. 2.7 into the weak form given in Eq. 2.5 and changing to matrix notation we obtain

$$\int_V \mathbf{c}^T \mathbf{N}^T \rho \mathbf{N} \ddot{\mathbf{a}} \, \mathrm{dV} + \int_V \mathbf{c}^T \mathbf{B}^T \boldsymbol{\sigma} \, \mathrm{dV} = \int_S \mathbf{c}^T \mathbf{N}^T \mathbf{t} \, \mathrm{dS} + \int_V \mathbf{c}^T \mathbf{N}^T \mathbf{b} \, \mathrm{dV}$$

Since $\mathbf{c}$ is arbitrary, the final expression for the FE-formulation is given by Eq. 2.8.

$$\left(\int_V \mathbf{N}^T \rho \mathbf{N} \, \mathrm{dV} \right) \ddot{\mathbf{a}} + \int_V \mathbf{B}^T \boldsymbol{\sigma} \, \mathrm{dV} = \int_S \mathbf{N}^T \mathbf{t} \, \mathrm{dS} + \int_V \mathbf{N}^T \mathbf{b} \, \mathrm{dV} \quad \Leftrightarrow \quad \mathbf{M}\ddot{\mathbf{a}} + \mathbf{f}_{int} = \mathbf{f}_{ext} \tag{2.8}$$

Here, the internal forces, f_{int}, are unknown. To determine them, an expression for the stresses, $\boldsymbol{\sigma}$, is needed, which is given by a constitutive relation. Eq. 2.8 provides a discretized approximation of the equation of motion, which converges towards the exact solution with decreasing element size. [3]

2.2 Constitutive Modeling

A constitutive model describes the relation between the stress, σ, and the strain, ϵ, in a material, which together with the kinematics relation, Eq. 2.6, and the FE-formulation, Eq. 2.8, provides a closed system of equations and the state of the body can be determined [3]. In this section, the constitutive model for paperboard will be described.

Assuming small deformations, the total strain can be divided into an elastic and a plastic part, $\epsilon = \epsilon^e + \epsilon^p$. In the elastic region, the body will recover to its original shape when unloaded. However, when loaded past the yield stress, σ_y, the plastic region is entered and permanent deformation arises, thus, the body will not return to its original shape [4].

In this project the paperboard material will be treated as an in-plane orthotropic elasto-plastic material with symmetric material response in tension and compression. However, for a more general description about the paperboard material mechanics and a more advance constitutive material model the reader is referred to [5].

2.2.1 Elasticity

During loading in the elastic region, i.e. $\sigma < \sigma_y$, the stress-strain relation is considered to be linear. For the purpose of describing this linear elasticity of paperboard, an orthotropic model is used, which entails three orthogonal planes of symmetry, due to the alignment of the fibers in the material, cf. Fig. 2.1b [6]. The constitutive relation is given by Hooke's law $\sigma = E\epsilon \Leftrightarrow \epsilon = \frac{1}{E}\sigma$, where E is Young's modulus, representing the stiffness of the material. Considering an orthotropic material, Hooke's law takes the following form in matrix notation

$$\boldsymbol{\epsilon}^e = \mathbb{C}\boldsymbol{\sigma} \quad \Leftrightarrow \quad \begin{bmatrix} \epsilon^e_{11} \\ \epsilon^e_{22} \\ \epsilon^e_{33} \\ 2\epsilon^e_{12} \\ 2\epsilon^e_{13} \\ 2\epsilon^e_{23} \end{bmatrix} = \begin{bmatrix} \frac{1}{E_1} & -\frac{\nu_{21}}{E_2} & -\frac{\nu_{31}}{E_3} & 0 & 0 & 0 \\ -\frac{\nu_{12}}{E_1} & \frac{1}{E_2} & -\frac{\nu_{32}}{E_3} & 0 & 0 & 0 \\ -\frac{\nu_{13}}{E_1} & -\frac{\nu_{23}}{E_2} & \frac{1}{E_3} & 0 & 0 & 0 \\ 0 & 0 & 0 & \frac{1}{G_{12}} & 0 & 0 \\ 0 & 0 & 0 & 0 & \frac{1}{G_{13}} & 0 \\ 0 & 0 & 0 & 0 & 0 & \frac{1}{G_{23}} \end{bmatrix} \begin{bmatrix} \sigma_{11} \\ \sigma_{22} \\ \sigma_{33} \\ \sigma_{12} \\ \sigma_{13} \\ \sigma_{23} \end{bmatrix} \tag{2.9}$$

Here, $\mathbb{C}$ is the linear elastic compliance or flexibility tensor, ν_{ij} are the Poisson's ratios and G_{ij} are the shear moduli. The index $i, j = 1, 2, 3$ denote the main directions in the material and for this particular case 1, 2, 3 refer to the Machine direction (MD), Cross-machine direction (CD) and Out-of-plane direction (ZD) respectively, as pictured in Fig. 2.1 [6].

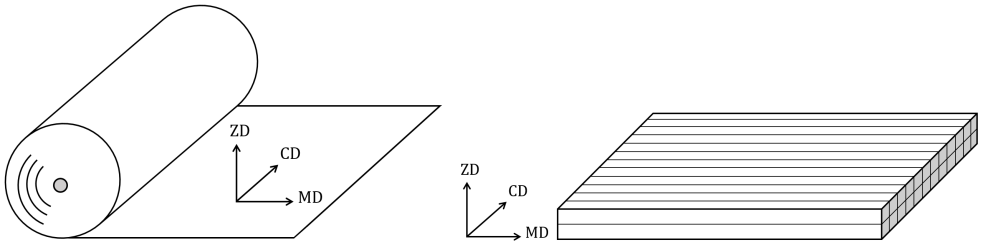

(a) Main directions of paperboard (b) Simplified sketch of the fiber alignment in paperboard

Figure 2.1: The orientation of the three main material axes in paperboard in correlation to the fiber alignment of the material.

Since thin sheets of paperboard are considered, plane stress conditions can be adopted, which means that the out-of-plane stress components $\sigma_{33} = \sigma_{13} = \sigma_{23} = 0$ resulting in $\nu_{13} = \nu_{23} = 0$ and $\epsilon^e_{33} = 0$. Thus, Eq. 2.9 can be reduced to the following

$$\boldsymbol{\epsilon}^e = \mathbf{C}\boldsymbol{\sigma} \quad \Leftrightarrow \quad \begin{bmatrix} \epsilon^e_{11} \\ \epsilon^e_{22} \\ 2\epsilon^e_{12} \end{bmatrix} = \begin{bmatrix} \frac{1}{E_1} & -\frac{\nu_{21}}{E_2} & 0 \\ -\frac{\nu_{12}}{E_1} & \frac{1}{E_2} & 0 \\ 0 & 0 & \frac{1}{G_{12}} \end{bmatrix} \begin{bmatrix} \sigma_{11} \\ \sigma_{22} \\ \sigma_{12} \end{bmatrix} \tag{2.10}$$

Inverting the flexibility matrix in Eq. 2.10 provides the stiffness matrix, $\mathbf{D}$, and the generalized Hooke's law can be written as

$$\boldsymbol{\sigma} = \mathbf{D}\boldsymbol{\epsilon}^e, \text{ where } \mathbf{D} = \mathbf{C}^{-1} = \frac{1}{1 - \nu_{12}\nu_{21}} \begin{bmatrix} E_1 & \nu_{21}E_1 & 0 \\ \nu_{12}E_2 & E_2 & 0 \\ 0 & 0 & G_{12}(1 - \nu_{12}\nu_{21}) \end{bmatrix} \tag{2.11}$$

We now have a complete model for the in-plane elastic properties of paperboard valid for $\boldsymbol{\sigma} < \boldsymbol{\sigma}_y$. [4]

2.2.2 Plasticity

During loading in the plastic region, i.e. $\sigma > \sigma_y$, the stress-strain relation is no longer linear due to the plastic strains that form in the body, thus no obvious relation between the stress and strain can be assumed. Paperboard is considered as an elasto-plastic material, which behavior is described in Fig. 2.2 [6]. The material is elastic with stiffness E until the initial yield stress, σ_{y0}, is reached, after that, plastic strains develop. Unloading from point *1*, the material responds elastically with stiffness E such that at complete unloading at point *2*, the residual strain corresponds to the plastic strain, ϵ_p, developed at point *1*. Loading again, from point *2*, the material behaves elastically until the stress reaches the new yield stress at point *1*. The value σ_y is therefore the current yield stress which, in general, is not equal to the initial yield stress. [4]

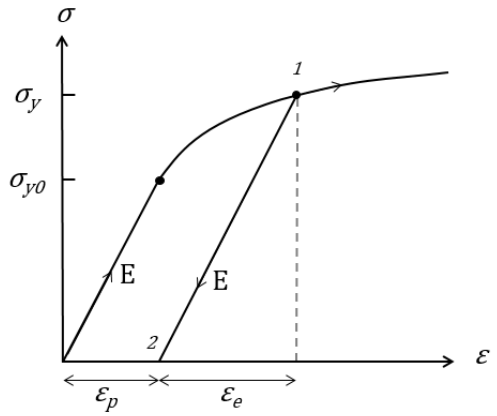

Figure 2.2: A stress-strain curve for an elasto-plastic material, such as paperboard.

Thus, the body will recover to its original shape when loaded such that $\sigma < \sigma_{y0}$ but return to a deformed shape when loaded with $\sigma > \sigma_{y0}$. Once the body is loaded with $\sigma > \sigma_{y0}$, the yield stress will increase to a new value σ_y. This material behavior, depicted in Fig. 2.2, is assumed to be time-independent, implying that the same response is obtained independent of the loading rate.

How the state of the body alters during plastic loading is modeled using a yield surface, which is defined by a yield function, describing the stresses in the material in the stress space, i.e. a coordinate system where the axis are given by σ_1, σ_2 and σ_3. So called hardening rules are then adopted, to properly model how the current yield stresses change due to plastic loading beyond σ_{y0}. [4]

Plasticity theory

A yield function, that describes the yield surface, is defined as $f = f(\boldsymbol{\sigma}, K_\alpha)$ where $K_\alpha = K_\alpha(\kappa_\beta)$ for $\alpha, \beta = 1, 2, 3...$ Here K_α are the hardening, or yield strength, parameters that describe the evolution of the yield surface, and κ_β are internal state variables representing the plasticity history, thus $\sigma_y = \sigma_{y0} + K_\alpha(\kappa_\beta)$. A stress state located inside the yield surface is elastic and for a stress state located on the surface, the yield point is reached and is therefore plastic. As the material keeps deforming the stress state remains on the yield surface, which is allowed to deform during loading. This deformation of the yield surface is described by the hardening parameters defined by a hardening rule. Stress states outside the yield surface are not allowed for time-independent models. [4]

Since the material behavior for paperboard is considered to be time-independent, the yield function has to fulfill the consistency relation $\dot{f} = 0$, in addition to $f = 0$, as shown in Eq. 2.12.

$$\dot{f} = \frac{\partial f}{\partial \boldsymbol{\sigma}} : \dot{\boldsymbol{\sigma}} + \frac{\partial f}{\partial K_\alpha} \dot{K_\alpha} = 0, \quad \text{where} \quad \dot{K_\alpha} = \frac{\partial K_\alpha}{\partial \kappa_\beta} \dot{\kappa_\beta} \tag{2.12}$$

As mentioned previously, the parameters κ_β describe the plasticity history and are therefore initially equal to zero and $\dot{\kappa_\beta} = 0$ yields during elastic loading. For the constitutive model of paperboard, the isotropic hardening rule is adopted for the yield surface, which gives $K_\alpha(\kappa_\beta) = K(\kappa)$.

An expression for the plastic strain rate, $\dot{\epsilon_p}$, is needed. Using the potential function approach the following definition is introduced

$$\dot{\epsilon_p} = \dot{\lambda} \frac{\partial g}{\partial \boldsymbol{\sigma}} \tag{2.13}$$

where $\dot{\lambda}$ is the plastic multiplier, and the dot notation denotes change of property rather than a time derivative [6], and $g = g(\boldsymbol{\sigma}, K)$ is an arbitrary potential function which here is chosen as $g = f$ for a simpler evaluation and ensuring that the thermodynamic considerations are met. Eq. 2.13 can be interpreted as an evolution law describing how the yield surface progresses in the stress space.

An evolution law for $\dot{\kappa}$ can now be defined, using the plastic multiplier

$$\dot{\kappa} = \dot{\lambda} k(\boldsymbol{\sigma}, K)$$

where $k(\boldsymbol{\sigma}, K) = 1$ is chosen, and the expression can be simplified to $\dot{\kappa} = \dot{\lambda}$. Using this, the consistency relation, stated in Eq. 2.12, can now be rewritten as

$$\frac{\partial f}{\partial \boldsymbol{\sigma}} : \dot{\boldsymbol{\sigma}} - H\dot{\lambda} = 0, \quad \text{where} \quad H = -\frac{\partial f}{\partial K_\alpha} \frac{\partial K_\alpha}{\partial \kappa_\beta} \tag{2.14}$$

Here, H represents the plastic modulus. To further describe the material behavior of paper, a suitable yield function must be determined. [4]

Hill's yield criterion

For this particular case, Hill's yield criterion is used to describe the yield surface, using the yield function

$$f(\boldsymbol{\sigma}, K) = (\sigma_{y0}^2 \mathbf{s} : \mathbb{P} : \mathbf{s})^{\frac{1}{2}} - \sigma_y(K) = 0 \tag{2.15}$$

where $\mathbf{s} = \boldsymbol{\sigma} - \text{tr}[\boldsymbol{\sigma}]\mathbf{I}$ are the deviatoric stresses, $\mathbb{P}$ is a fourth order tensor, σ_{y0} and $\sigma_y(K)$ represent the initial yield stress and current yield stress respectively. $\mathbb{P}$ is defined as

$$\mathbb{P} = \begin{bmatrix} \tilde{\mathbf{P}} & \mathbf{0} \\ \mathbf{0} & \tilde{\mathbf{Q}} \end{bmatrix}, \quad \text{with} \quad \tilde{\mathbf{P}} = \begin{bmatrix} F+G & -F & -G \\ -F & F+H & -H \\ -G & -H & G+H \end{bmatrix}, \quad \tilde{\mathbf{Q}} = \begin{bmatrix} 2L & 0 & 0 \\ 0 & 2M & 0 \\ 0 & 0 & 2N \end{bmatrix}$$

where F, G, H, L, M and N are parameters characterizing orthotropic material defined as

$$\begin{aligned} F &= \tfrac{1}{2}\left(\tfrac{1}{R_{22}^2} + \tfrac{1}{R_{33}^2} - \tfrac{1}{R_{11}^2}\right) & L &= \tfrac{3}{2R_{23}^2} \\ G &= \tfrac{1}{2}\left(\tfrac{1}{R_{11}^2} + \tfrac{1}{R_{33}^2} - \tfrac{1}{R_{22}^2}\right), & M &= \tfrac{3}{2R_{13}^2} \\ F &= \tfrac{1}{2}\left(\tfrac{1}{R_{11}^2} + \tfrac{1}{R_{22}^2} - \tfrac{1}{R_{33}^2}\right) & N &= \tfrac{3}{2R_{112}^2} \end{aligned}$$

Here R_{ij} for $i = 1, 2, 3$ and $j = 1, 2, 3$ are the anisotropic yield stress ratios.

Combining Hill's yield criterion with the isotropic hardening rule, it follows that the position and shape of the yield surface remains fixed, whereas the size of the yield surface changes. An image of an arbitrary yield curve for Hill's criterion with isotropic hardening can be seen in Fig. 2.3. The dotted line in Fig. 2.3 represents the deformed yield curve after further loading beyond the initial yield stress. From the symmetry of the yield curve in respect to each coordinate axis, it can be observed that the Hill's yield criterion does not distinguish tension from compression.

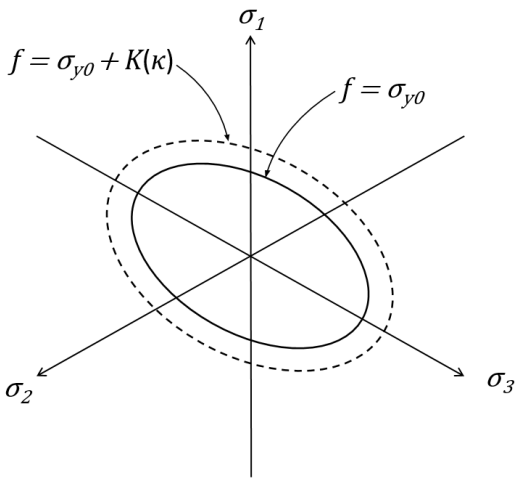

Figure 2.3: A yield curve in the stress space for Hill's criterion with isotropic hardening. The dotted line represents the deformed yield curve after further loading beyond the initial yield stress.

As the yield surface is now established, the plastic strain rate from Eq. 2.13 and the plastic modulus from Eq. 2.14 can be computed by deriving the yield function provided by Hill's yield criterion in Eq. 2.15.

$$\begin{aligned} \dot{\epsilon^p} &= \dot{\lambda}\frac{\partial f}{\partial \boldsymbol{\sigma}} = \dot{\lambda}\frac{\sigma_{y0}^2}{\sigma_y}\mathbb{P} : \mathbf{s} \\ \frac{\partial f}{\partial K} &= -1 \;\Rightarrow\; H = \frac{\partial K}{\partial \kappa} = \frac{\mathrm{d}\sigma_y(\epsilon_{eff}^p)}{\mathrm{d}\epsilon_{eff}^p} \end{aligned} \tag{2.16}$$

Here ϵ^p_{eff} is the effective plastic strain.

Finally, the elasto-plastic stiffness tensor can be determined. Recalling that $\epsilon = \epsilon^e + \epsilon^p$ which gives the strain rates $\dot{\epsilon} = \dot{\epsilon^e} + \dot{\epsilon^p}$, the linear elastic stress rate can be expressed using Hooke's law as $\dot{\sigma} = \mathbb{D} : (\dot{\boldsymbol{\epsilon}} - \dot{\boldsymbol{\epsilon}^p})$. By combining this with the consistency relation in Eq. 2.14 and the quantities in Eq. 2.16 and with some rearranging of terms, the elasto-plastic relation between the stress rate and the total strain rate can be determined, i.e. $\dot{\boldsymbol{\sigma}} = \mathbb{D}^{ep} : \dot{\boldsymbol{\epsilon}}$ providing the elasto-plastic stiffness tensor as

$$\mathbb{D}^{ep} = \mathbb{D} - \frac{1}{A}\left(\frac{\sigma_{y0}^2}{\sigma_y}\right)^2 (\mathbb{D} : (\mathbb{P} : \mathbf{s})) \otimes ((\mathbb{P} : \mathbf{s}) : \mathbb{D}), \quad \text{where} \tag{2.17}$$

$$A = H + \left(\frac{\sigma_{y0}^2}{\sigma_y}\right)^2 (\mathbb{P} : \mathbf{s}) : (\mathbb{D} : (\mathbb{P} : \mathbf{s}))$$

We have now obtained the constitutive material model for the elastic and plastic properties of paperboard, valid for all σ which can be used to solve for the internal forces, f_{int}, in the FE-formulation, Eq. 2.8. [4]

2.3 Numerical methods

In this project the FE-software Abaqus/Standard version 2017 and 2020, is employed for modeling the structural part of the FSI-problem. In the following subsections, some of the modeling tools provided by Abaqus/Standard are explained as well as some brief numeric theory applied by the software.

2.3.1 Meshing

Rigid bodies

When modeling a rigid body in Abaqus/Standard, a so-called discrete mesh can be used. This is applied when the deformation of the part at hand can be considered negligible compared to other deformable parts in the domain. The relative positions of the nodes and elements that are part of the rigid body remain constant throughout a simulation. This saves computational power, since element-level calculations, such as the element stiffness, are not performed for rigid parts. A rigid body can only undergo rigid body movement, which is equally computational expensive as for a deformable body. Thus, a rigid body takes a passive role in the simulation, only modeling contact conditions between itself and other, moving parts in the domain. One can choose between several element types, when modeling a 3D rigid body. In this project, the two element types used are the R3D4 and R3D3, pictured in Fig. 2.4a-b. The R3D4 element type, is a 4-node 3D bilinear rigid quadrilateral element and R3D3 is a 3-node 3D rigid triangular facet. The elements are 2D but can model a 3D geometry. [7]

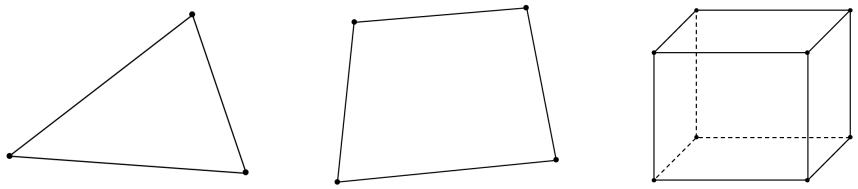

(a) R3D3 (b) R3D4 (c) C3D8R/C3D8I

Figure 2.4: The three element types used in this project to mesh the domain in Abaqus/Standard. R3D3 and R3D4 are 3- and 4-node rigid body elements respectively, and C3D8R and C3D8I are 8-node, deformable body elements.

Deformable bodies

For a deformable body, element-level calculations are performed at every time step and nodes are allowed to move relative to each other. There is a wide range of different element types for deformable bodies in Abaqus/Standard that allow for several kinds of physics and deformations, offering different numerical methodologies. In this project, the element types C3D8R and C3D8I were mainly used, pictured in Fig. 2.4c. Both element types are 8-node linear, i.e. first-order, hexahedral elements, where the C3D8R-element uses reduced integration whereas the C3D8I uses full integration and incompatible modes, for calculating the element properties.[7]

When computing the element-level properties, such as the deformation and stiffness, integration is required to obtain the FE equations, i.e. numerical integration. Gauss integration is used for this purpose in Abaqus/Standard. In numerical integration, the following approximation is made

$$I = \int_a^b f(\xi)\,\mathrm{d}\xi \simeq \sum_{i=1}^{n} f(\xi_i) H_i$$

where I is the quantity to determine, $f(\xi)$ is an arbitrary function, ξ are integration points and H_i are weights. For Gauss integration these integration points and weights are determined and optimized such that a given polynomial is integrated exactly. From this, the positions of the integration points, called *Gauss points*, are known before the numerical integration is conducted, thus the Gauss integration provides an exact integration of a polynomial of the order $2n - 1$, for n integration points. [3]

In reduced integration only one Gauss point is used, which can give rise to zero strains causing uncontrolled distortion of the mesh called "Hourglassing". In Abaqus/Standard, this is managed by a function called Hourglass control which adds an additional artificial stiffness to the elements. Since only one integration point is used, the computational time is reduced compared to full integration. In full integration several Gauss points are used for the numerical integration providing higher accuracy and avoiding Hourglassing. How the integration points are located in 2D elements for reduced and full integration can be seen in Fig. 2.5, the same distribution of the Gauss points apply to the faces of 3D elements. [7]

In addition to the full integration, C3D8I also uses Incompatible modes, which are internally added degrees of freedom. If the elements have approximately rectangular shape, the incompatible mode elements, perform almost as well second-order elements. [7]

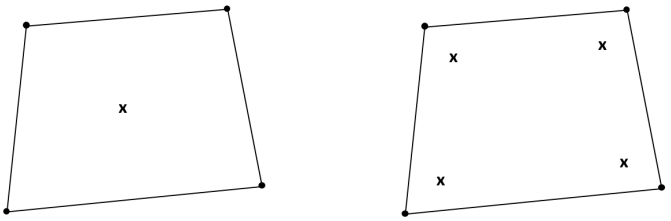

(a) Reduced integration (b) Full integration

Figure 2.5: The location of the Gauss points in reduced and full integration. The same principle applies to the faces of 3D elements.

2.3.2 Contact definitions

In Abaqus/Standard, the surface-to-surface mechanical contact property model is called pressure-overclosure relationship. This relation is defined in terms of the distance between the two surfaces versus the contact pressure. The distance is measured perpendicular to the master surface (defined by the user) and is called overclosure, or clearance, depending on if the distance between the surfaces is smaller, or greater, than a specified tolerance. The pressure-overclosure relation specifies that no contact pressure is transmitted unless the surfaces are closer than the specified tolerance distance and, when in contact, there is no limit to the magnitude of the contact pressure transmitted. [7]

In this project, only so-called "soft" contact is employed, thus the pressure-overclosure relationship follows a curve, which is defined by the user. In contrast, for the "hard" contact, the pressure-overclosure follows the Dirac delta function. Here, linear and exponential pressure-overclosure will be used.

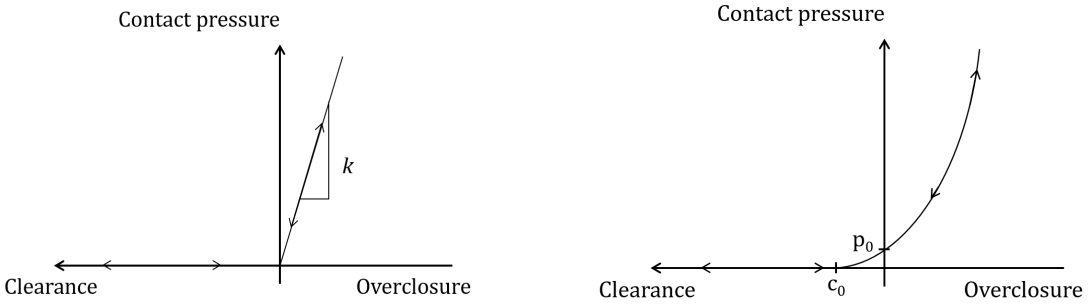

(a) Linear (b) Exponential

Figure 2.6: The pressure-overclosure relationships for defining contact between surfaces in Abaqus/Standard.

For a linear relationship, the surfaces transmit contact pressure when the overclosure between them is greater than zero and increasing linearly as the overclosure increases. For the linear pressure-overclosure relationship, the curve describing this behavior is defined by the first point, which by default is at the origin and the user-defined slope k, as pictured in Fig. 2.6a. As for the exponential version, contact pressure is introduced when the clearance between the surfaces reduces to c_0. The contact pressure increases exponentially as the distance continues to decrease, cf. Fig. 2.6b. The exponential curve,

describing this behavior, is defined by the two parameters: c_0 and p_0 which are the contact tolerance and contact pressure for zero clearance, defined by the user.

In this kind of contact models, Abaqus/Standard assumes per default frictionless contact. However, a friction model can be included by the user. [7]

2.3.3 Numerical solver

In Abaqus/Standard, the Newton method is used to solve the non-linear equations. To solve the equations, the solver divides the solution into increments called time steps, which in turn are subdivided into smaller time steps. The solver moves on to the next time step, when the previous one has converged.

Take the example pictured in Fig. 2.7. The solver is currently at a load f_n yielding a displacement a_n and the goal is to calculate the displacement, a_{n+1}, in the next time step, as the load increases to f_{n+1}. Starting at a_n, the tangent is calculated and used to predict a^1, by calculating the residual $f_{n+1} - f(a^1)$. Starting now from a^1, the tangent and the residual is once again calculated and a^2 is determined. In this fashion, the solver iterates until the residual is small enough. As the residual is smaller than the tolerance value, equilibrium is considered to be reached and $a_{n+1} = a^3$ is adopted [4]. In Abaqus/Standard, the solver also checks that the last displacement correction $a_{res} = a^3 - a^2$ is small compared to the total displacement increment $a^3 - a_n$. If a_{res} is too large, another small time step is performed. Both convergence checks need to be fulfilled in order to claim full convergence for the current time step [7].

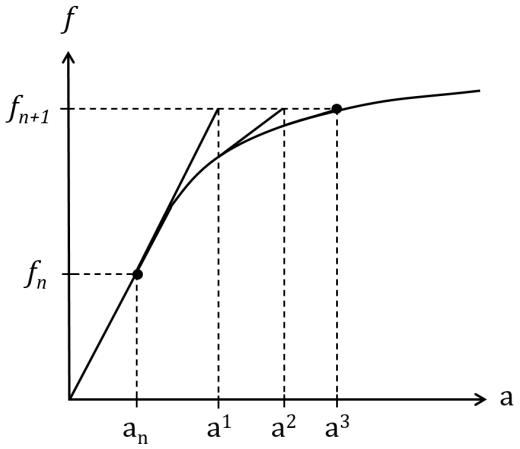

Figure 2.7: The principle of how the Newton solution scheme works.

Chapter 3

Fluid Mechanics

Fluid mechanics is the field within physics describing the behavior of a fluid flow. As a subclass of mechanics, continuity and balance equations are used to solve problems within blood flow, turbines, airplanes and engines to name a few. By subdividing the flow domain in sufficiently small volumes, or cells, for which the equations are solved and then assembling these into larger systems, the final solution is obtained. The space discretization is, as for a structural problem, handled by a mesh and using Computational Fluid Dynamics, CFD, the equations are discretized and solved. This is a powerful tool, for analyzing problems with strong non-linearities and large systems of equations.

3.1 Fundamental fluid mechanics

The governing equations that describe a fluid flow are the conservation laws of physics, ensuring conservation of mass, momentum and energy within the fluid. [8]

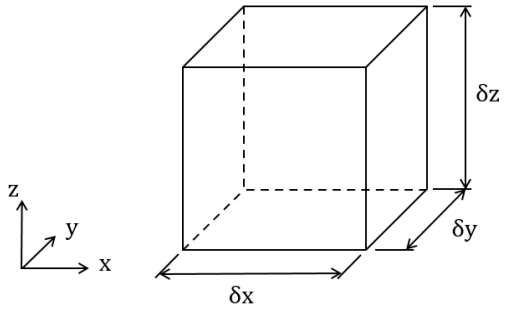

Figure 3.1: A sketch of a fluid element for deriving the conservation laws.

The fluid will be regarded as a continuum and the behavior of the fluid will be described in terms of properties averaged over a suitable large number of molecules. A small fluid element, as shown in Fig. 3.1, with the sides δx, δy and δz, whose macroscopic properties are not effected by single molecules, will be used in the following derivations. [9]

3.1.1 Mass conservation

The equation describing the conservation of mass, states that the rate of increase of mass in a fluid element is equal to the net rate of flow of mass into the fluid element. The mass flow rate across the face of the element is given by the product of area, density, and the velocity component normal to the face. Taking account for the sign of each component, depending on if the flow enters or exits the element, the continuity equation can be written as stated in Eq. 3.1 below.

$$\frac{\partial \rho}{\partial t} + \nabla \cdot (\rho \mathbf{u}) = 0 \tag{3.1}$$

Here ρ is the density of the fluid and $\mathbf{u}$ is the velocity vector with the components $\mathbf{u} = (u, v, w)$. Eq. 3.1 is the unsteady, three-dimensional mass conservation equation, the so-called continuity equation, for a compressible fluid.

For an incompressible fluid the density is assumed to be constant and Eq. 3.1 can be simplified, taking the new form given by Eq. 3.2. [9]

$$\nabla \cdot \mathbf{u} = 0 \tag{3.2}$$

3.1.2 Momentum equation

The momentum equation states that the rate of change of momentum of a fluid element is equal to the sum of the forces acting on the element (Newton's second law). The forces are divided into body forces and surface forces, where the body forces are included as source terms in the equations. The surface forces are highlighted as separate terms and derived from the surface stresses in terms of viscous stresses and pressure (normal to the surface), multiplied by the area of the fluid element. Thus, the momentum equations take the following form:

$$\rho \frac{Du}{Dt} = \frac{\partial(-p + \tau_{xx})}{\partial x} + \frac{\partial \tau_{yx}}{\partial y} + \frac{\partial \tau_{zx}}{\partial z} + S_{Mx} \tag{3.3}$$

$$\rho \frac{Dv}{Dt} = \frac{\partial(\tau_{xy})}{\partial x} + \frac{\partial(-p + \tau_{yy})}{\partial y} + \frac{\partial \tau_{zy}}{\partial z} + S_{My} \tag{3.4}$$

$$\rho \frac{Dw}{Dt} = \frac{\partial(\tau_{xz})}{\partial x} + \frac{\partial \tau_{yz}}{\partial y} + \frac{\partial(-p + \tau_{zz})}{\partial z} + S_{Mz} \tag{3.5}$$

τ_{ij} denotes the viscous stress tensor, where i represents the direction along which the stress component acts. The body forces, S_{Mi}, are given as source terms of momentum per unit volume per unit time. Here, $\frac{D\bullet}{Dt}$ is equal to $\frac{\partial \bullet}{\partial t} + \nabla \cdot (\bullet \mathbf{u})$ and denotes the total derivative. Eq. 3.3-3.5 ensure the conservation of momentum for each component in a three dimensional flow and is valid for any fluid in any general motion. [9]

Assuming an isotropic fluid were the viscous stresses are proportional to the rate of deformation is called a Newtonian fluid. Using this approximation, $\boldsymbol{\tau}$ can be simplified using the velocity gradients and constants of proportionality. After some rearrangement,

Eq. 3.3-3.5 take a new form Eq. 3.6-3.8, called the *Navier-Stokes equations* which are key equations within the field of fluid dynamics. Here, incompressibility is again assumed.

$$\rho\frac{Du}{Dt} = -\frac{\partial p}{\partial x} + \nabla\cdot(\mu\nabla u) + S'_{Mx} \tag{3.6}$$

$$\rho\frac{Dv}{Dt} = -\frac{\partial p}{\partial y} + \nabla\cdot(\mu\nabla v) + S'_{My} \tag{3.7}$$

$$\rho\frac{Dw}{Dt} = -\frac{\partial p}{\partial z} + \nabla\cdot(\mu\nabla w) + S'_{Mz} \tag{3.8}$$

Here μ is the dynamic viscosity and $\mathbf{S'_M}$ are modified momentum sources, defined as the sum of the previous source terms and the smaller contributions to the viscous stress terms.

Using the *Reynolds number*, these equations can be made dimensionless. The Reynolds number gives the ratio of inertial to viscous forces, indicating whether the flow is laminar or turbulent. [9]

3.1.3 Energy equation

Using the first law of thermodynamics, the energy conservation equation can be derived, which states that the rate of change of energy of a fluid element is equal to the rate of change of heat addition plus the rate of work performed on the fluid element. The rate of work performed by surface forces is expressed using the product of the force and velocity component in the direction of the force, adding the work exerted by surface stresses, yields the total rate of work. The net rate of heat transfer, in each direction, to the fluid element is given by the difference of heat flow into one face of the element and the heat loss across the opposite face. Using Fourier's law of heat conduction, the heat flux is related to the local temperature gradient, ∇T, and the conductivity, k. Defining the total energy, E, of the fluid element as the sum of internal (thermal) energy and the kinetic energy, the energy equation is obtained as stated in Eq. 3.9 below. The potential energy is regarded as a gravitational force, thus included as a source term, S_E.

$$\rho\frac{DE}{Dt} = -\nabla\cdot(p\mathbf{u}) + \nabla\cdot(\boldsymbol{\tau}\cdot\mathbf{u}) + \nabla\cdot(k\nabla T) + S_E \tag{3.9}$$

In conclusion, this provides a set of five partial differential equations, that describe the motion of the fluid in three dimensions by determining the velocity field and pressure and temperature distribution of the fluid for a given set of boundary conditions and initial conditions.

Among the unknowns, in these five equations, are the thermodynamic variables ρ, p and T, which require a sixth equation linking them together. This equation, based on thermodynamic equilibrium, is called the equation of state and can be differently formulated depending on the case and assumptions that can be made. E.g. for a perfect gas, the equation of state is the ideal gas law, Eq. 3.10.

$$p = \rho RT \tag{3.10}$$

Here, R is the ideal gas constant. [9]

3.2 Numerical methods

In this project, the CFD software used to solve the fluid part of the FSI-problem is STAR-CCM+, version 15.04 and 15.06. In the following subsections some numeric theory and modeling tools, provided by STAR-CCM+, will be explained.

3.2.1 Modeling turbulence

Consider the continuity and momentum equations, 3.1 and 3.3-3.5, which describe the instantaneous behavior of the flow. Taking the time average of the turbulent behavior, can give insight on the general behavior of the flow and reducing the sensitivity to small alterations of the initial conditions. Introducing a separation of the velocity, **u** with the components u, v and w, and pressure, p, into a fluctuating, u', v', w' and p', and mean part, U, V, W and P, as

$$\mathbf{u = U + u'} \quad u = U + u' \quad v = V + v' \quad w = W + w' \quad p = P + p'$$

Applying the rules of time-averaging, the continuity and momentum equations can be rewritten as shown in Eq. 3.11-3.13, and are called the *Reynolds-averaged Navier-Stokes equations*, or RANS for short.

$$\rho\frac{DU}{Dt} = -\frac{\partial P}{\partial x} + \nabla\cdot(\mu\nabla U) - \left(\frac{\partial(\rho\overline{u'^2})}{\partial x} + \frac{\partial(\rho\overline{u'v'})}{\partial y} + \frac{\partial(\rho\overline{u'w'})}{\partial z}\right) \tag{3.11}$$

$$\rho\frac{DV}{Dt} = -\frac{\partial P}{\partial y} + \nabla\cdot(\mu\nabla V) - \left(\frac{\partial(\rho\overline{u'v'})}{\partial x} + \frac{\partial(\rho\overline{v'^2})}{\partial y} + \frac{\partial(\rho\overline{v'w'})}{\partial z}\right) \tag{3.12}$$

$$\rho\frac{DW}{Dt} = -\frac{\partial P}{\partial z} + \nabla\cdot(\mu\nabla W) - \left(\frac{\partial(\rho\overline{u'w'})}{\partial x} + \frac{\partial(\rho\overline{v'w'})}{\partial y} + \frac{\partial(\rho\overline{w'^2})}{\partial z}\right) \tag{3.13}$$

The over-bar denotes the mean value over time. The procedure of time-averaging introduces new terms involving products of fluctuating velocities associated with convective momentum transfer, representing turbulent stresses, and are called the *Reynolds-stresses*. When trying to determine these, several new unknowns need to be introduced, hence not solving the problem of trying to reduce the number of unknowns in the system of equations. Thus, different turbulence models have been established over time, to model the Reynolds stresses. One of the most commonly used is explained below. [9]

The k-ϵ model

The k-ϵ model is a two-equation model, entailing that two transport equations are utilized to solve for the turbulent quantities: the turbulent kinetic energy, k, and the dissipation rate of the turbulent kinetic energy, ϵ. Using these two quantities, the turbulent viscosity, μ_t is determined, making it possible to compute the Reynolds stresses using the Boussinesq hypothesis. [9]

The transport equation for the turbulent kinetic energy is derived by multiplying each of the Navier–Stokes equations, Eq. 3.6-3.8, by the corresponding fluctuating velocity component, i.e. the x-component equation is multiplied by u' etc., and adding the three results. Repeating this procedure for the RANS equations, Eq. 3.11-3.13, and subtracting this result from the one obtained by the Navier-Stokes equations, one obtains the equation for turbulent kinetic energy k, stated in Eq. 3.14. In a similar manner the transport model equation for ϵ can be deducted, as shown in Eq. 3.15. However, the model equation for ϵ is best viewed as entirely empirical, since ϵ is not a physical property in the classical sense. [10]

$$\frac{D(\rho k)}{Dt} = \nabla \cdot \left(\frac{\mu_t}{\sigma_k} \nabla k \right) + 2\mu_t S_{ij} \cdot S_{ij} - \rho\epsilon \tag{3.14}$$

$$\frac{D(\rho \epsilon)}{Dt} = \nabla \cdot \left(\frac{\mu_t}{\sigma_\epsilon} \nabla \epsilon \right) + 2C_{1\epsilon} \frac{\epsilon}{k} \mu_t S_{ij} \cdot S_{ij} - C_{2\epsilon} \rho \frac{\epsilon^2}{k} \tag{3.15}$$

Here, S_{ij} is the mean rate of deformation, defined as $S_{ij} = \frac{1}{2}\left(\frac{\partial U_i}{\partial x_j} + \frac{\partial U_j}{\partial x_i} \right)$ and μ_t is the turbulent viscosity, determined by the turbulent viscosity theory, specifying $\mu_t = \rho C_\mu \frac{k^2}{\epsilon}$. C_μ, σ_k, σ_ϵ, $C_{1\epsilon}$ and $C_{2\epsilon}$ are the five dimensionless model constants, determining the k-ϵ model.

Finally the system is closed by using the Boussinesq relation, Eq. 3.16, to determine the Reynolds stresses.

$$-\rho \overline{u_i' u_j'} = 2\mu_t S_{ij} - \frac{2}{3}\rho k \delta_{ij} \tag{3.16}$$

Where δ_{ij} is the Kronecker delta.

By introducing wall-damping functions, and including molecular viscosity, to the original Eq. 3.14 and Eq. 3.15, the k-ϵ model copes better with low Reynolds number flows and captures near-wall effects more accurately. This version of the k-ϵ model is called the *realizable k-ϵ model*. [9]

3.2.2 The boundary layer and wall treatment

Boundary layer theory

Close to the wall, the flow is influenced by viscous effects and does not depend on free stream parameters. This region is called the boundary layer and requires extra attention when modeling the flow. The velocity profile in the boundary layer is described using the dimensionless length scale y^+ (wall units) and the dimensionless velocity u^+, defined in Eq. 3.17.

$$y^+ = \frac{u_\tau y}{\nu}, \quad u^+ = \frac{U}{u_\tau} \tag{3.17}$$

Here, U is the mean flow velocity, ν is the kinematic viscosity, u_τ is the friction velocity defined as $\sqrt{\tau_w/\rho}$, with τ_w representing the wall shear stress.

The boundary layer is sub-divided into three different regions, in terms of y^+. Values $y^+ < 5$ correspond to the *viscous sub-layer* and $y^+ > 30$ define the log-law region. The region $5 < y^+ < 30$ is called the *buffer layer*, as seen in Fig. 3.2.

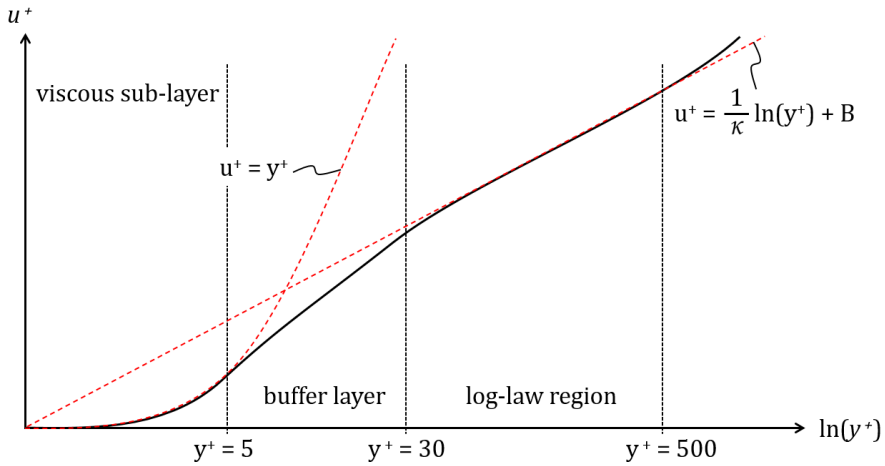

Figure 3.2: The velocity profile in the boundary layer, accompanied by the corresponding numeric approximations.

In the region closest to the wall, the viscous sub-layer, the velocity can be approximated using the linear relation

$$u^+ = y^+$$

For the log-law region, it has been empirically shown that relation between u^+ and y^+ can be described using the logarithmic relationship

$$u^+ = \frac{1}{\kappa}\ln(y^+) + B$$

where κ and B are constants which are determined by measurements and vary with the smoothness of the wall. [9]

The buffer layer, between the viscous sub-layer and the log-law region, is the transition region between the viscosity-dominated and the turbulence-dominated part of the boundary layer. Here, no obvious relation between y^+ and u^+ exists, making it harder to model the behavior of the velocity in this part of the flow. [10]

Wall treatment functions in STAR-CCM+

Smaller mesh cells near the wall are necessary, to properly resolve the behavior of the velocity profile explained above. Prism cells allow for this necessary refinement in the direction perpendicular to the wall, while keeping the cell size parallel to the surface large enough to avoid excessive cell count. The first cell of the prism layer, i.e. the cell closest to the wall, should correspond to the y^+ value for best accuracy and resolution of the flow. The total thickness of the prism layer should correspond to the thickness of the boundary layer.

STAR-CCM+ provides different kinds of wall treatment that model the velocity profile and various parameters for the turbulence such as production and dissipation, near the wall, which is necessary when dealing with turbulent flows. Depending on the y^+ value of the problem, different choices of wall treatment can be made. For $y^+ > 30$, High Y+ Wall Treatment, i.e. a coarse mesh, is optimal and for $y^+ < 5$, i.e. a fine mesh, Low Y+ Wall Treatment is recommended. A third option, All Y+ Wall Treatment, is a hybrid approach that emulates the Low Y+ Wall Treatment for fine meshes, and the High Y+ Wall Treatment for coarse meshes on a cell-to-cell basis.

3.2.3 Modeling the mesh morphing

The movement or deformation of the mesh, or mesh morphing, is accounted for by using a set of control points, which are superimposed onto the mesh vertices. Each of these control points are defined using the coordinates of vertices that lie on mesh boundaries and are associated with a displacement vector that defines the displacement of the point within each time-step. Using these control points and their known displacements, the morpher function generates an interpolation field which is applied to all mesh vertices in the region. This procedure allows the morpher to adapt the original mesh in accordance with the movement of the boundaries. In STAR-CCM+, there are two different interpolation methods that can be used to morph the mesh, the RBF method and the B-spline method.

The RBF (Radial Basis Functions) method uses multi-quadratic radial B-splines, which belong to the family of polynomial interpolation functions. The interpolation field is formed using the control points and their displacements, to determine the final mesh deformation. By default, one control point per mesh vertex is created. To achieve an optimal number of control points, a "thin-out" procedure is adopted to reduce the number of points and lower the run-time, by using an estimated deformation of the mesh, while maintaining an acceptable mesh quality.

The B-spline method utilizes an adaptive interpolation algorithm, using multi-level cubic B-splines. Starting from a coarse control-point grid and propagating down to finer grids, until the residual error is within the limits of the user-specified morpher tolerance, the B-spline method achieves an accurate interpolation field from which the mesh deformation is then determined. Since a hierarchical refinement approach is adopted, the number of control points used is automatically optimized, hence the run-time is kept to a minimum. The B-spline method scales better than the default RBF method in many circumstances and it can also better preserve meshes that contain prism layers [11].

3.2.4 Overset method

When dealing with a geometry containing parts that move relative to each other, overlapping grid techniques, also called overset mesh methods, are very useful to discretize the computational domain. This methodology allows different parts to be meshed individually, avoiding issues that arise when one continuous grid for the whole domain is used, which would require re-meshing and extreme mesh morphing for larger relative movement between parts in the domain. When using overlapping methods, there will always be a background region, which is the static part of the domain, enclosing smaller regions of interest, which move relative to the background and each other, meshed by

the overset mesh. The component meshes can exchange flow field information from one mesh to the other through the overlap region. [12]

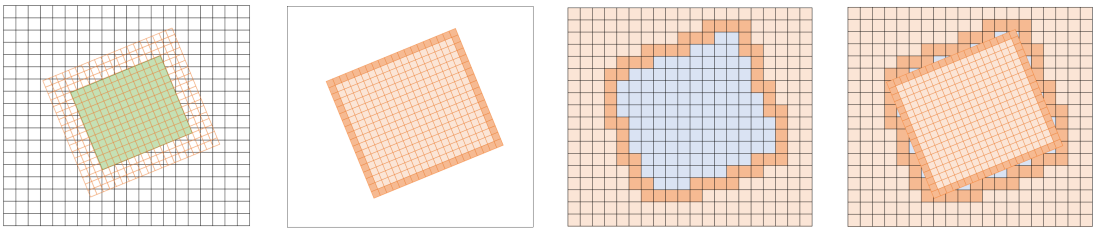

(a) Square meshed with overset method (b) Cell types for the overset mesh (c) Cell types for the background mesh (d) The full domain

Figure 3.3: A visualization of how the different cell types in an overset methodology can be distributed. Light orange are active cells, dark orange represent acceptor cells and blue answer to the passive cells.

There are three different types of cells involved in the overset method: active, passive and acceptor cells. As an example, consider a square moving across a simple domain, meshed using the overset method, Fig. 3.3a. The active cells, colored light orange in Fig. 3.3b-d, are the cells where the flow equations are solved and are located both in the background mesh and in the overset region. Thus, one part of the domain will be solved in the background region and one part will be solved in the overset region. The passive cells, colored blue in Fig. 3.3c-d, are the ones in the background region, overlapped by the overset, where no flow equations need to be solved. However, the passive cells become active once the overset region moves. The acceptor cells, colored dark orange in Fig. 3.3b-d, separate the active and passive cells. These cells make the exchange of information between the meshes, in both directions, possible. The process which determines the type of the cells in the domain is called the "Hole-cutting" process. [12]

The data transfer

The data transfer occurs at the boundary of the overlapping region, using the acceptor cells. To solve the flow equations the value of each cell centroid is needed, which is calculated using the fluxes through the cell faces. However, for the acceptor cells, one flux is undetermined, since it has no neighboring cell at the boundary, Fig. 3.4a. This is solved by introducing a set of ghost cells, that form an outer layer, surrounding the overset boundary, Fig. 3.4b. The missing neighbor for the acceptor cells is created. The centroid of the ghost cell is determined by using the value of three active cell centroids of the background mesh. These cells are called donor cells and are selected such that the triangle formed by their centroids encloses the ghost cell centroid, Fig. 3.4c. Using a distance weighted average, the ghost cell centroid is determined, yielding the last flux for the acceptor cells and a set of closed system of equations, Fig. 3.4d. For this type of data transfer being able to work, matching cell sizes between the component meshes, is required. If the mesh cell sizes differ too much, problem with finding donor cells can arise and interpolating the data between the meshes may become inaccurate. [11]

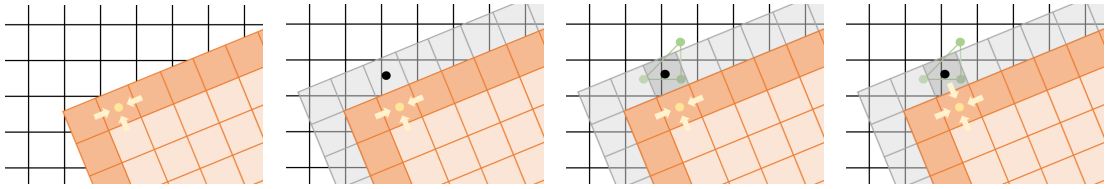

(a) The acceptor cells (b) The ghost cells (c) Determining centroid of ghost cell (d) Determining flux to acceptor cell

Figure 3.4: The figure shows how data transfer is performed between the background mesh (white) and the overset mesh (orange) using ghost cells (gray). The yellow arrows represent the cell face fluxes and the circular dots answer to the cell centroids.

3.2.5 Contact definition

When defining contact conditions between bodies and overset regions, one approach provided by STAR-CCM+ is called ZeroGap interface. This type of interface automatically creates a ZeroGap wall boundary for each region. During the simulation, the overset hole-cutting process will use these ZeroGap wall boundaries to define contact. When the distance between two of these boundaries is less than the user defined limit (in terms of cell layers), the cells in this gap are inactivated and treated as a wall, thus temporarily preventing the flow between the surfaces and the gap effectively closes. Isolated cell islands surrounded only by ZeroGap boundaries are detected automatically by the solver and inactivated. This approach yields an effective procedure for treating small gaps and direct contact between bodies, since gaps are closed and opened continuously during the simulation as the bodies in the domain are moving relative to each other. [11]

3.2.6 Solution interpolation

When dealing with moving and deforming parts in the domain it is sometimes necessary to update or replace the old mesh with a new one, which requires an interpolation technique for mapping the data between the old and the new mesh. In STAR-CCM+ there are mainly two methods for this kind of data mapping: Nearest neighbor and Higher-order stencil.

The nearest neighbor interpolation option maps the data from the old mesh to the new one, by comparing the cell centroids. The cell centroid of the new mesh obtains the solution data retrieved from the old cell centroid closest to the new one. This method is fast; however, it does not provide a smooth interpolation of the results.

The higher-order stencil maps the solution data from the old mesh to the new one by enforcing a stencil, a set of cells and faces. This method uses a distance-weighted, least-square interpolation, yielding a smooth interpolation of the solution data and is therefor recommended for transient analyses. [11]

3.2.7 Numerical solver

To solve the equations of motion for the flow domain at hand, and handling the strong non-linearities, an iterative approach is required. For the set-ups described in this project,

the "Segregated Flow" solver is employed in STAR-CCM+. This formulation uses a collocated variable grid to discretize the domain and conservation equations Eq. 3.1, 3.3-3.5, where the convection fluxes are approximated by a second order upwind scheme [11]. Since a collocated grid is used, the values for the pressure and velocity components, used for solving the discretized transport equations, are stored in the center of each cell face, as opposed to a staggered grid where the velocity components are stored around the cell faces instead [9]. To prevent unphysical checkerboarding of the pressure, i.e. obtaining zero pressure gradients due to linear interpolation of the velocities from the cell center to the cell face, the Rhie-Chow pressure-velocity coupling is applied [11].

The SIMPLE algorithm is invoked for solving the discretized momentum equations and calculating the pressure and velocity components [11]. Initially the momentum equations are solved using an arbitrarily guessed pressure field, obtaining the velocity components. A pressure correction equation is used to obtain the correct pressure and the momentum equations are solved again, to update the velocity component values. In this iterative, predictor-corrector approach, the transport equations are solved, and the correct pressure and velocity field is obtained. [9]

To ensure convergence and a numerically stable solution, the Gauss-Seidel relaxation scheme is employed [11]. This iteration method uses information from both the current and previous time step to determine the values for the pressure and velocity in the current time step, ensuring a faster convergence. [9]

3.3 Fluid-Structure Interaction

Fluid-Structure Interaction, FSI, is a multi-physics coupling between the laws of fluid dynamics and structural mechanics. It describes the coupled problem where a fluid flow introduces a stress state along the surface of a structural body, causing deformations that in turn affects the flow, thus describing the interaction between a fluid flow and a deformable structural body. To describe these physical phenomena correctly, highly advanced solution procedures are required to account for the strong non-linearities and the full behavior of the two-field interactions. [13]

Two different methods can be applied to solve the equations of motion: monolithic or partitioned solution schemes. Both methods aim to solve the same set of equations with respect to the boundary conditions at hand but do so in opposite fashions. A monolithic solution scheme solves all equations simultaneously with one solver, while a partitioned solution scheme uses two separate solvers. This entails that the flow field does not change while the solution of the structural equations is determined and vice versa. Since the monolithic approach solves all equations simultaneously, a mathematically more accurate solution is obtained. However, solving these kinds of system of equations is a hard task to conduct, which is why partitioned schemes are usually adopted when solving FSI problems. Since two separate solvers are used, it is easier to individually update each software making sure state-of-the-art solvers are employed. [14]

Partitioned solution schemes are further divided into two groups: *explicit schemes* and *implicit schemes*. Schematic flow charts of the principle of these couplings can be seen in Fig. 3.5. The explicit partitioned schemes, sometimes called weak coupling, solve the FSI problem in a staggered manner without convergence checks on a domain level, while the implicit (strong coupled) partitioned schemes iterate in each time step, making sure convergence is reached across the domain. However, convergence checks are preformed

within the fluid and solid solver in both approaches. [1]

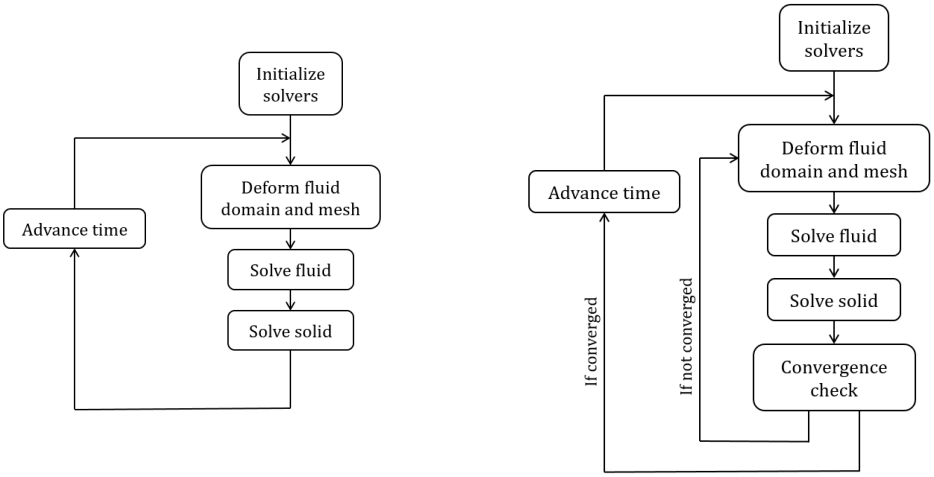

(a) Explicit method (b) Implicit method

Figure 3.5: Simplified flow charts for how an (a) explicit and an (b) implicit coupling works in principle.

As mentioned previously, in this project the software STAR-CCM+ is used to solve the flow and for the structural part, Abaqus/Standard is employed. The coupling is strong, and an implicit partitioned scheme is used. Based on the pressure and wall shear stress exported by STAR-CCM+, Abaqus/Standard determines the deformation of the solid body. The deformation is imported to STAR-CCM+, which is used to adapt and update the flow. This exchange of data is repeated several times in each time step.

Chapter 4

Previous work

To solve the problem of jams arising while evacuating the confetti, several simulations have previously been performed at Tetra Pak®. In these simulations, different variations of the geometry for the knife roller were evaluated, to test if these variations could prevent some of the problems that occur when the confetti are evacuated from the machine. Some of the different geometry variations are illustrated in Fig. 4.1. The geometries that were tested are a 1D offset of the knife tubes, to prevent the confetti from exiting through the opposite knife. Ripples and bumps on the inside surface of the main pipe were also introduced, to see if the sticking can be prevented. These different geometries were mainly simulated as steady-state simulations, to analyze the air flow alone. Some of the cases were also run as transient simulations, without the confetti, to analyze how the rotation of the knife roller affects the air flow. Only one of the geometries were run with a confetti as an FSI-simulation.

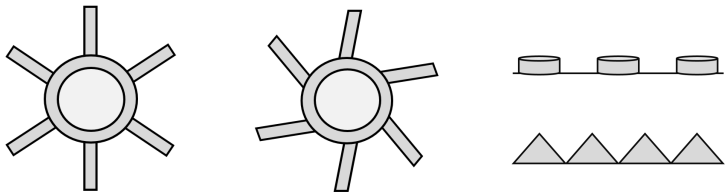

(a) Original design (b) 1D offset (c) Ripples

Figure 4.1: An illustration of the different geometries of the knife roller, previously tested at Tetra Pak®. The illustrations show the knife roller from the front to display the angle of the knifes. The ripples are introduced along the inside surface of the main pipe.

Since most of these simulations are performed without confetti, it is of interest to investigate how the confetti change the airflow and how they are transported and deformed. Understanding how the confetti behave, could give insight on how the jams arise. Therefore, the Pre-existing model was developed. Using a simple domain, error sources due to geometry can be avoided, making it easier to develop a model for the behavior of the confetti and its deformation in the airflow.

4.1 The Pre-existing Model

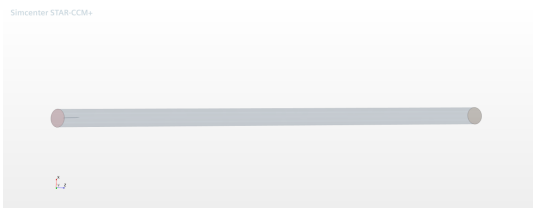

(a) The pipe with the confetti to the left.

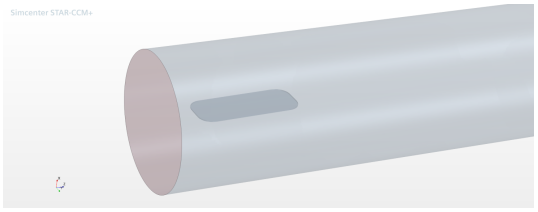

(b) Close up of the confetti at the inlet of the pipe.

Figure 4.2: The geometrical set-up of the Pre-existing model

The Pre-existing model, developed and provided by Tetra Pak®, is set up accordingly: it models one single confetti in a straight pipe, as pictured in Fig. 4.2. The confetti is of rectangular shape and consists of paperboard with the dimensions 35x12.1 mm and is 0.35 mm thick. The pipe is 1.01 m long and has a radius of 21 mm. Using Abaqus/Standard, the geometries are defined, and the domain is set up, which is then imported in STAR-CCM+.

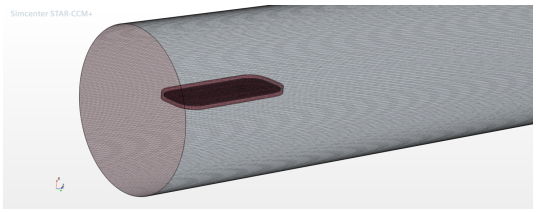

(a) Mesh of pipe and confetti

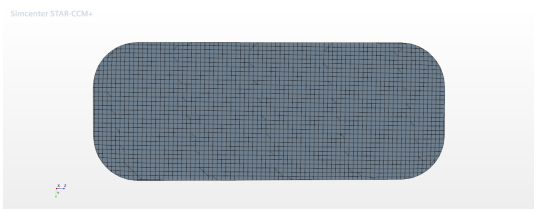

(b) Mesh of confetti

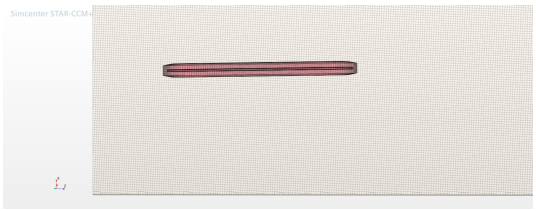

(c) Cross-section of the domain

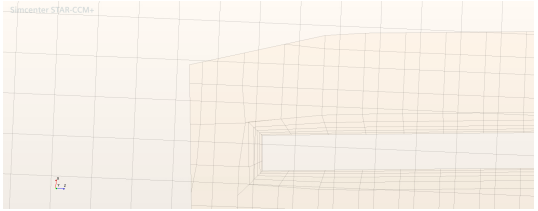

(d) The overset mesh

Figure 4.3: The mesh of the Pre-existing model

The two parts are meshed using a trimmed cell mesher with a base cell size of 0.4 mm generating 26 000 000 cells for the pipe, see Fig. 4.3. An overset region, inflated 1.0 mm in respect to the confetti surface, is created for the confetti, enabling the confetti to have its own mesh and travel through the mesh of the flow domain. The overset mesh has the same cell size and type as the rest of the domain resulting in 44 000 cells for the confetti including the overset mesh. The same mesh element size is applied for all parts, to reduce error while interpolating the solution between the two meshes, see Fig. 4.3. Prism layers are only introduced along the boundaries of the confetti, but not along the pipe wall.

The following boundary conditions are imposed: The pipe wall and confetti surface are set to no-slip surfaces. The inlet velocity is evenly distributed across the inlet surface of

the pipe and set to 5.0 m/s. A zero pressure outlet is applied to the far end of the pipe. Initially the confetti is non-deformed and is placed in the center of the pipe at the inlet, parallel to the pipe wall. All contacts are set to frictional contacts with surface-to-surface properties applied.

To model the flow, ideal gas properties are assumed for the air and laminar flow conditions are applied. The Segregated flow solver is used, and an implicit unsteady solver of 1st order is adopted for the temporal discretization to model the physical time and to control the time-step size. An adaptive time-step size is chosen with the minimum step size set to 1e-4 s. A mesh morpher is activated, using the RBF method, to handle the deformation of the mesh of the confetti during the simulations.

For the structural part of the simulation, Abaqus/Standard uses the Newton method to solve the non-linear equations for the deformation, based on the pressure and wall shear stress provided by STAR-CCM+. The same time-step sizes are applied for this part of the solver, as set in STAR-CCM+.

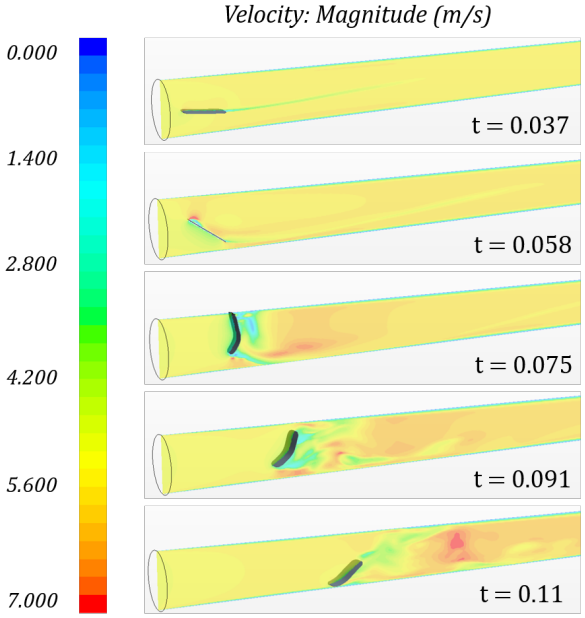

Figure 4.4: The figures show the velocity contour plot in a cutting plane, provided by the Pre-existing model. One can see how the confetti deforms and travels through the pipe.

This set-up provides a model that captures the behavior of the confetti and that is numerically stable to simulate the deformation of the confetti, its movement through the pipe and its contact with the pipe wall, as well as the air flow itself. Fig. 4.4 shows the velocity contour plot of the beginning of the simulation in a cutting plane. One can clearly see how the confetti is deformed by the flow and its contact to the pipe wall, and how it travels through the pipe. It can also be observed how the air flow is affected mainly downstream of the confetti.

Chapter 5

Computational set-up

5.1 Developing the Final Model

In the process of developing an FSI-model that simulates two confetti in the final T-junction pipe geometry, the Pre-existing model is expanded by the author by means of several smaller sub-steps, described below. An overview of all the FSI-models created, in the process to obtain the Final model, can be seen in Fig. 5.1. Each model is described further in the following subsections.

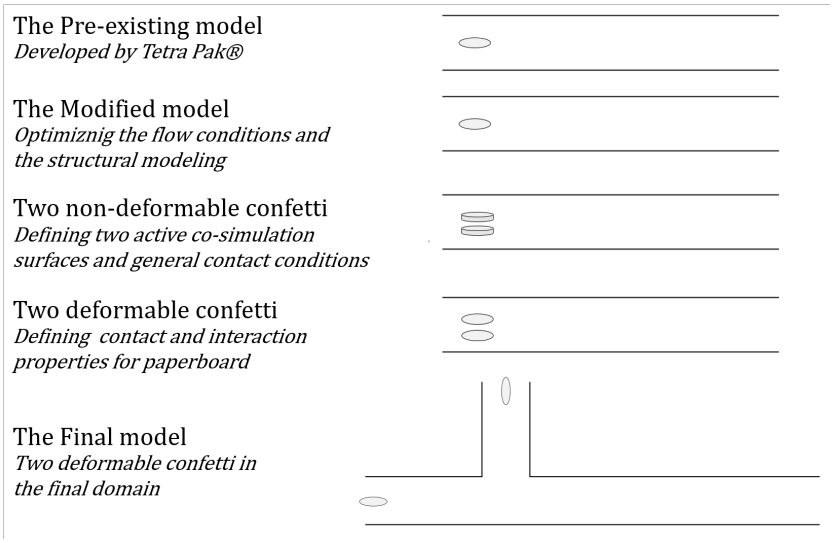

Figure 5.1: Overview of the development process.

5.1.1 The Modified Model

First, the Pre-existing model is investigated, making sure that the optimal settings for the flow case are chosen for this kind of simulation, without changing the geometry of the domain. A few alterations are made, resulting in the *Modified model*.

The changes entail activating the function "Close proximity". This allows more active cells in the overset mesh between the moving body and the boundary and helps to prevent mesh intersector failure when the overset region overlaps the physical boundaries of

the background [11]. The solver interpolation method is changed from "Nearest Neighbor" to "Higher-Order Stencil" and the mesh morpher method is changed from RBF to the B-Spline method. A morpher tolerance of 1e-8 is used to avoid negative volume cells and "Linear Fitter" is activated, enabling the model to simulate both displacement and deformation. The Reynolds number for this flow case is given by:

$$\mathrm{Re} = \frac{\rho u D}{\mu} = \frac{1.204\ \mathrm{kg/m^3} \cdot 5.000\ \mathrm{m/s} \cdot 0.042\ \mathrm{m}}{1.855 \cdot 10^{-5}\ \mathrm{Ns/m^2}} \approx 14\,000$$

Since it exceeds 2300, which is the critical Reynolds number for a pipe flow [8], a turbulence model is activated. The k-ϵ model is chosen since it performs well for simple pipe flows [10], using the default settings for the k-ϵ model provided by STAR-CCM+.

Furthermore, the frictional constant is changed from 0.4 to 0.2, which according to practical experience, is a more realistic value for paperboard interacting with metal. The element type, used to mesh the confetti in Abaqus/Standard, is altered from a C3D8R element type to a C3D8I element type. This allows higher accuracy since the C3D8I uses full integration, instead of reduced integration as C3D8R does.

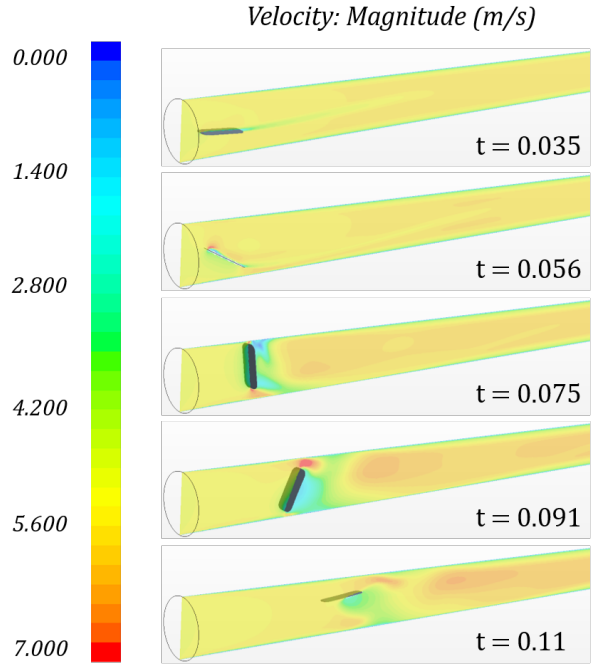

Figure 5.2: The figures show the velocity contour plot provided by the Modified Model.

Fig. 5.2 shows the velocity contour plot in a cutting plane of the Modified Model. One can see how the confetti deforms less, which coincides better with what is expected, due to the new element type used to mesh the confetti in Abaqus/Standard. It can also be observed how there are less turbulent vortices in the flow downstream of the confetti, compared to the initial case, due to the time averaging the k-ϵ model imposes on the flow. Based on the Reynolds number, the pipe flow is undoubtedly turbulent, indicating the flow behavior observed in the Pre-existing model to be inaccurate.

The model to simulate one single confetti in a straight pipe, is now substantially improved, since the more accurate B-spline morphing method now can be used without the simulation crashing and the new contact conditions are considered as more realistic.

Also, the new element type employed in Abaqus/Standard, ensures higher accuracy of the deformation of the confetti. Therefore, this model is used as a base for future steps in the development process.

5.1.2 Introducing two confetti

Two non-deformable confetti

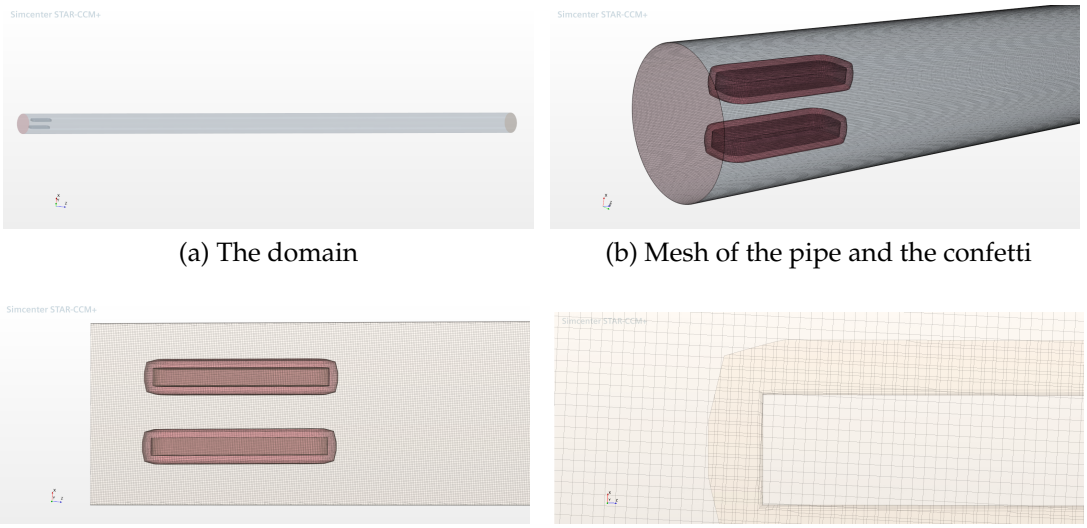

(a) The domain

(b) Mesh of the pipe and the confetti

(c) Cross-section of the domain

(d) The overset mesh

Figure 5.3: The set-up for two paperboard confetti in a straight pipe.

Using the Modified model, focus is now directed to the number of active FSI-surfaces. A second confetti, thus a second part for the co-simulation, is introduced to the model. The thickness of both confetti is increased, and the material is changed to steel to ensure rigid body movement, to reduce potential problems regarding deformation. Images of the mesh and the geometric set-up can be seen in Fig. 5.3. Using the same initial and boundary conditions as for the case with one confetti established in the Modified Model, a numerically stable model that can handle two non-deformable confetti is obtained. Fig. 5.4 shows the velocity contour plot of this simulation.

Due the heavy material applied to the confetti, the inlet velocity, and thus the flow, is too slow to affect the confetti. They simply drop to the bottom of the pipe and bounce off each other a few times. The model obtained can handle two active co-simulation surfaces and is considered good enough to describe the interaction between two confetti to move forward to the next step in the development process.

Here, the contact conditions were assessed. Initially, in the Pre-exiting and Modified model, a linear pressure-overclosure contact condition, with the slope $k = 1e8$ was set. However, to see if the contact could be modeled more realistically, different values for the slopes were tested and an exponential pressure-overclosure contact was also investigated. In the end, a linear pressure-overclosure relation with $k = 1e9$ performed the best, in terms of numerical stability and realistically capturing of the behavior of and contact between the confetti. Data from the contact analysis can be found in appendix A.

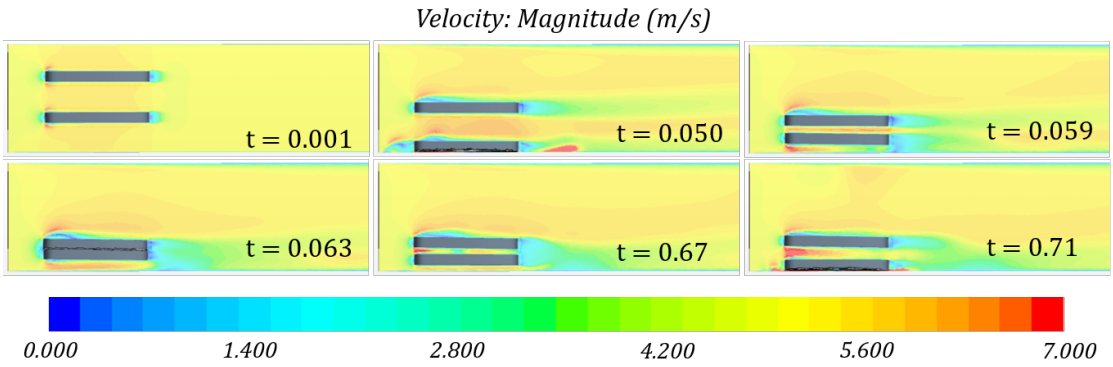

Figure 5.4: The velocity contour plot for two non-deformable confetti in a straight pipe, side view.

Two deformable confetti

The set-up with two co-simulation surfaces, is now used to take the next step. The initial thickness is chosen, in Abaqus/Standard, for both confetti and the material is set to paperboard, the geometry of this model can be seen in Fig. 5.5a. The same settings for the flow and solid solver are used as previously and the same type of mesh is applied as well, as shown in Fig. 5.5b-c. Thus, a model that simulates two deformable confetti of paperboard, in a straight pipe is obtained.

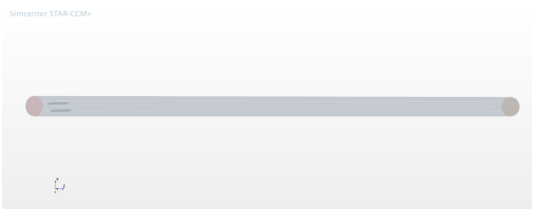

(a) The domain

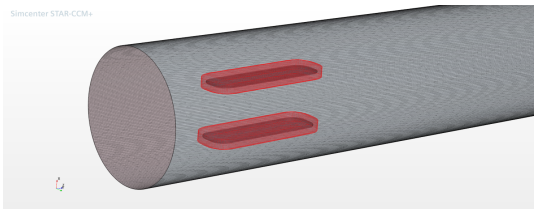

(b) Mesh of the pipe and the confetti

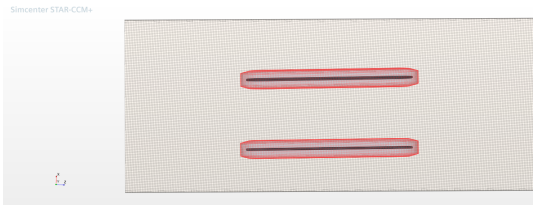

(c) Cross-section of the domain

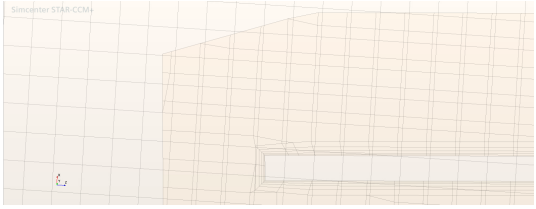

(d) The overset mesh

Figure 5.5: The set-up for two paperboard confetti in a straight pipe.

The interaction between the confetti seems to be captured well. Fig. 5.6 shows the velocity contour plot in a cutting plane of this simulation case. One can see how the upper confetti is efficiently transported by the flow, while the lower confetti initially gets stuck to the wall of the pipe.

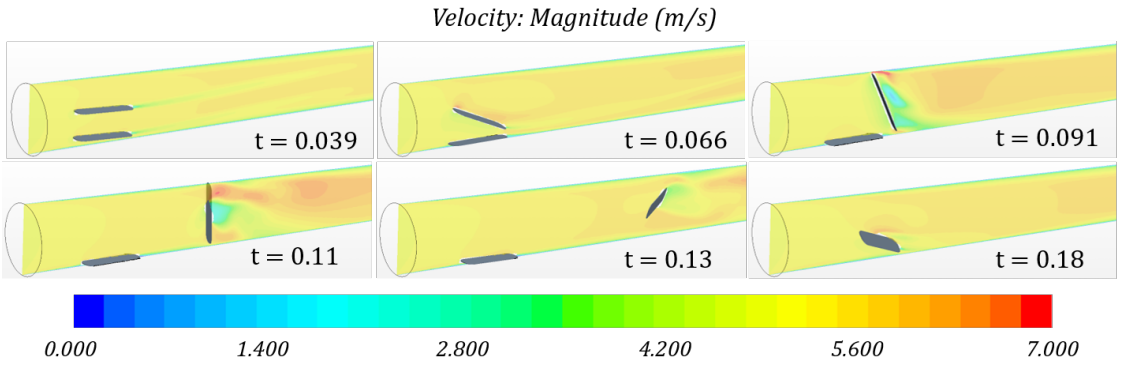

Figure 5.6: The velocity contour plot for two deformable paperboard confetti in a straight pipe.

5.1.3 Mesh sensitivity analysis

To ensure a solution that is mesh-independent and not too computational expensive, a mesh sensitivity analysis is conducted. The mesh analysis is performed on the Modified Model since it is the simplest of cases run. To ensure that the cases with the different meshes are comparable, and that differences are a result of the mesh and not the movement of the confetti, steady state simulations were conducted with the confetti placed to be static, in the middle of the pipe. A set of five different meshes were tested for two different orientations of the confetti, as pictured in Fig. 5.7. The meshes included in the study can be seen in Table 5.1. Here, Mesh 4 is the mesh that has previously been used in the Pre-existing model.

Table 5.1: An overview of the mesh sensitivity analysis.

	Base cell size	Number of cells per diameter	Total number of cells
Mesh 1	1.6 mm	28.3	370 000
Mesh 2	0.8 mm	56.6	2 800 000
Mesh 3	0.6 mm	75.5	6 600 000
Mesh 4	0.4 mm	113	22 000 000
Mesh 5	0.2 mm	227	176 000 000

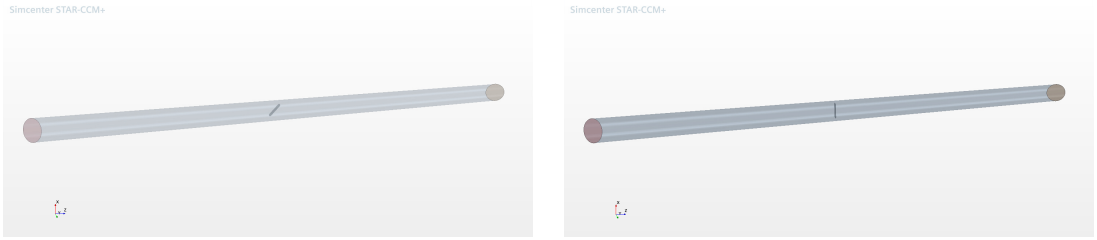

(a) Confetti at 45° in middle of pipe

(b) Confetti at 90° in middle of pipe

Figure 5.7: The two geometries used for the, steady state, mesh sensitivity analysis.

The coarsest and the finest mesh, Mesh 1 and Mesh 5, can be seen in Fig. 5.8 and 5.9.

(a) Confetti at 45° (b) Confetti at 45°

(c) Confetti at 90° (d) Confetti at 90°

Figure 5.8: Images of the coarsest mesh tested, Mesh 1, for the two different confetti orientations.

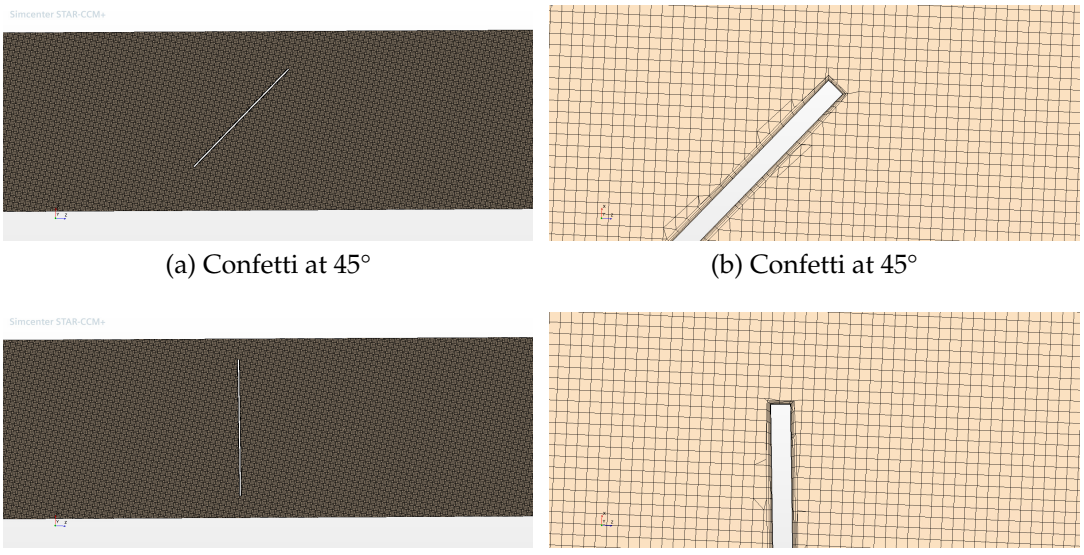

(a) Confetti at 45° (b) Confetti at 45°

(c) Confetti at 90° (d) Confetti at 90°

Figure 5.9: Images of the finest mesh tested, Mesh 5, for the two different confetti orientations.

For the study, the velocity was tracked along two different lines, one placed upstream and one placed downstream of the confetti, as shown in Fig. 5.10a-b. The pressure and wall shear stress were averaged over the top and bottom surface of the confetti, as defined in Fig. 5.10c. Since, the pressure and wall shear stress are the parameters exported to Abaqus/Standard, it is of interest to ensure mesh independence for these parameters.

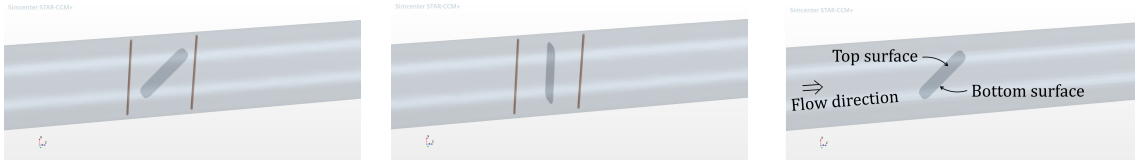

(a) Probe lines, confetti at 45° (b) Probe lines, confetti at 90° (c) Definition of top and bottom surface

Figure 5.10: The figures show the line probes along which the velocity was measured and how the top and bottom surface of the confetti is defined for measuring the pressure and wall shear stress in the mesh sensitivity analysis.

The results from the mesh sensitivity analysis are gathered in Fig. 5.11-5.14.

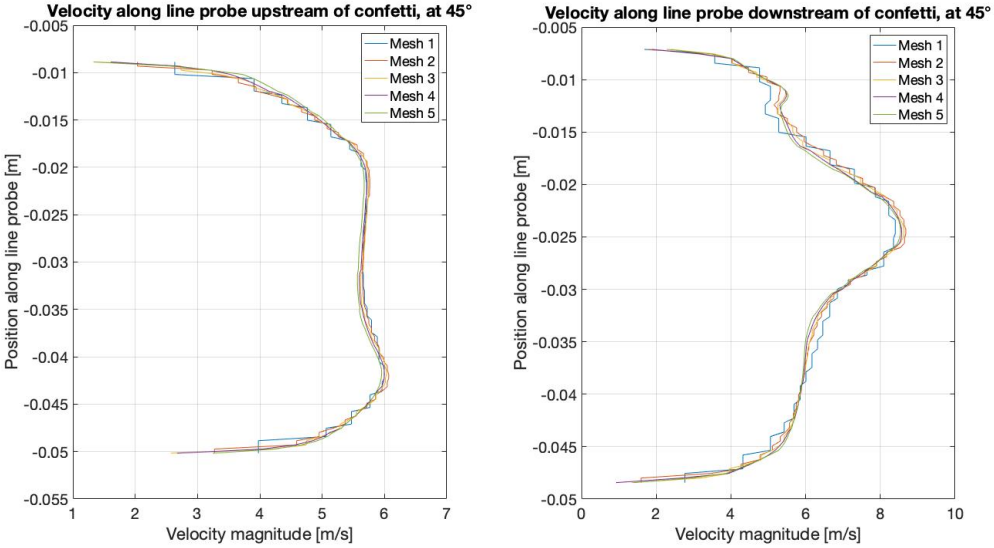

(a) Velocity profile upstream (b) Velocity profile downstream

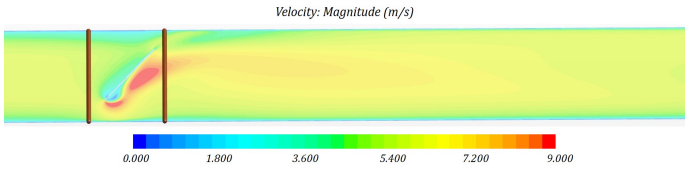

(c) Line probe in velocity contour plot

Figure 5.11: The velocity profile given by the line probes, displayed in (c), for the confetti at 45°.

The velocity, measured up- and downstream of the confetti, can be seen in Fig. 5.11 and 5.12, where the velocity profiles are plotted alongside the velocity contour plot. In both cases, it is clearly visible that Mesh 1 and Mesh 2 are not sufficient to resolve the full velocity profile, compared to Mesh 4 and Mesh 5.

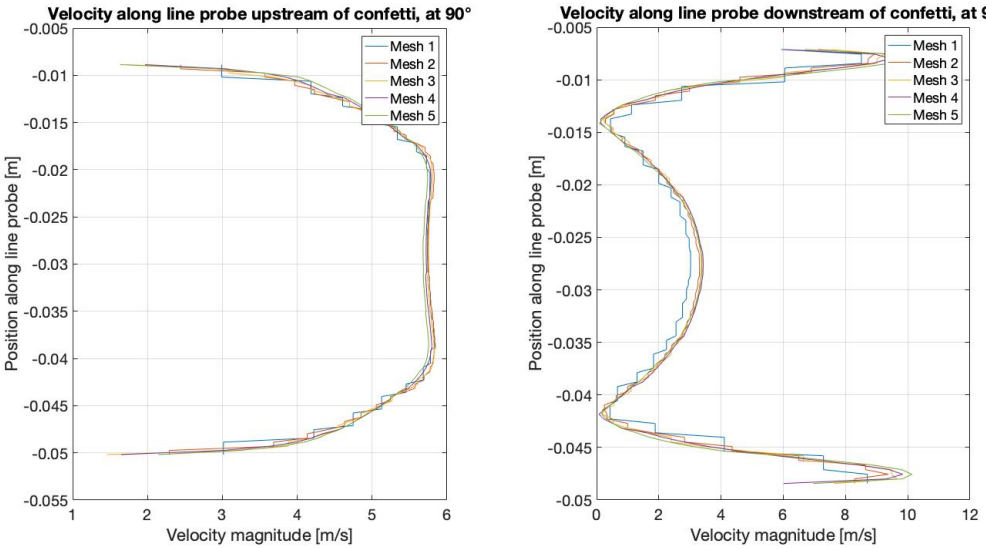

(a) Velocity profile upstream

(b) Velocity profile downstream

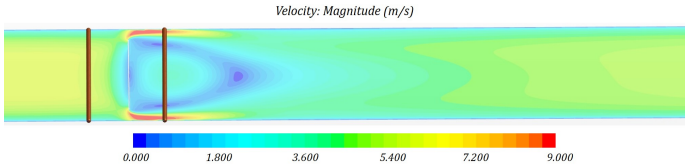

(c) Line probe in velocity contour plot

Figure 5.12: The velocity profile given by the line probes, displayed in (c), for the confetti at 90°.

In Fig. 5.13 the average pressure, measured across the bottom and top surfaces of the confetti can be seen for each case. The graphs are normalized against the value provided by Mesh 5. Compared to Mesh 5, Mesh 1 deviates the most in all cases.

In Fig. 5.14 the average wall shear stress, measured across the bottom and top surfaces of the confetti can be seen for each case. The graphs are normalized against the value provided by Mesh 5. As for the pressure, Mesh 1 generally deviates most from Mesh 5. For the wall shear stress on the bottom surface for the confetti at 90° we see deviations of as much as 50 %. However, for the other three cases, all meshes provide about the same value, while Mesh 1 deviates with less than 10 %.

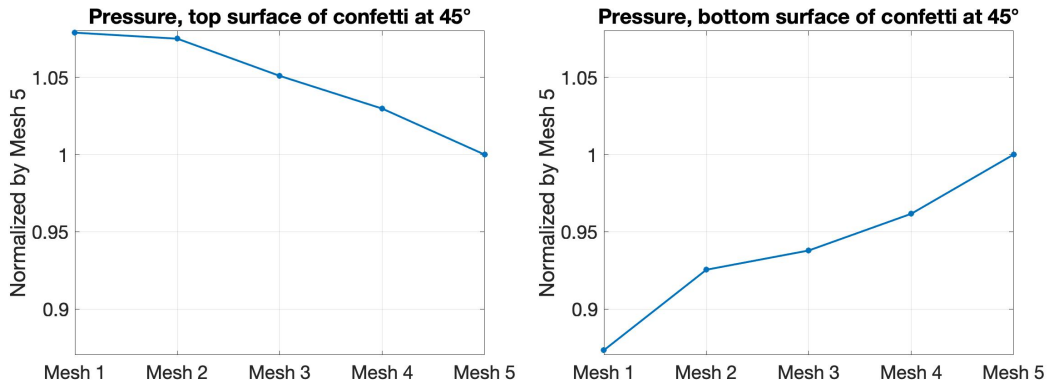

(a) Pressure, top surface at 45°

(b) Pressure, bottom surface at 45°

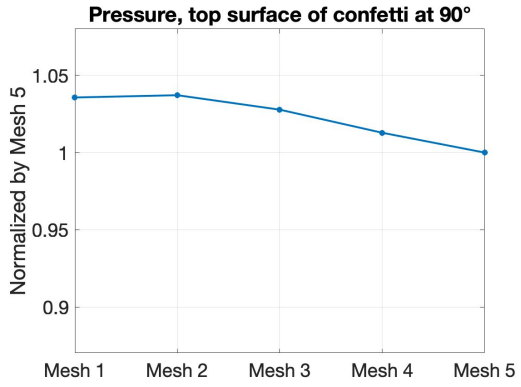

(c) Pressure, top surface at 90°

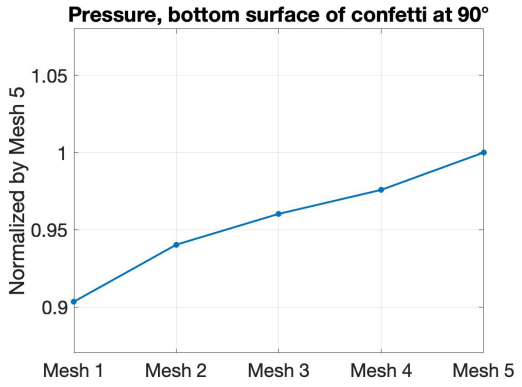

(d) Pressure, bottom surface at 90°

Figure 5.13: The graphs depict the average pressure on the top and bottom surface for each confetti configuration and mesh size. The values are normalized against Mesh 5.

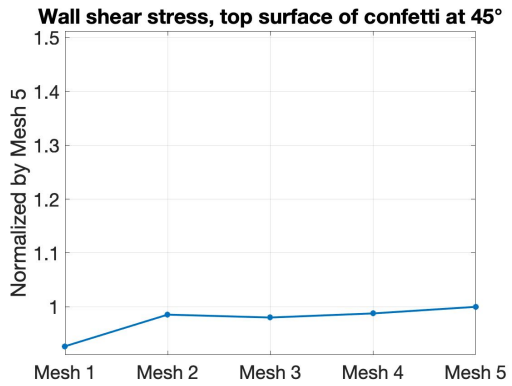

(a) Wall shear stress, top surface at 45°

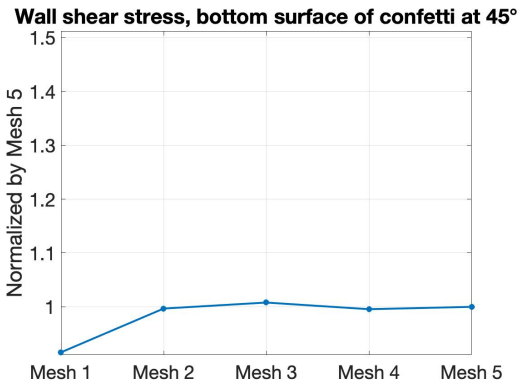

(b) Wall shear stress, bottom surface at 45°

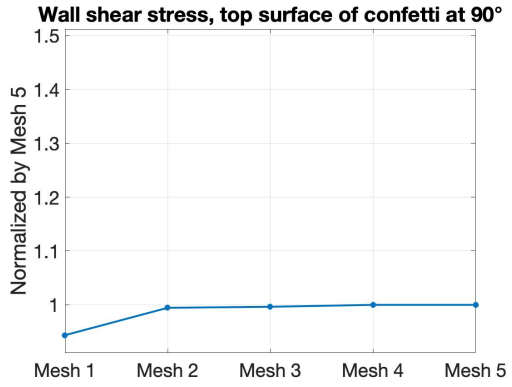

(c) Wall shear stress, top surface at 90°

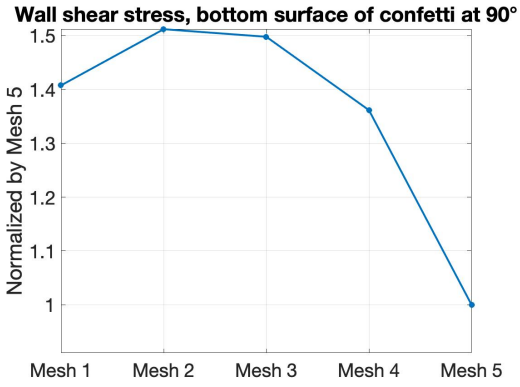

(d) Wall shear stress, bottom surface at 90°

Figure 5.14: The graphs depict the average wall shear stress on the top and bottom surface for each confetti configuration and mesh size. The values are normalized against Mesh 5.

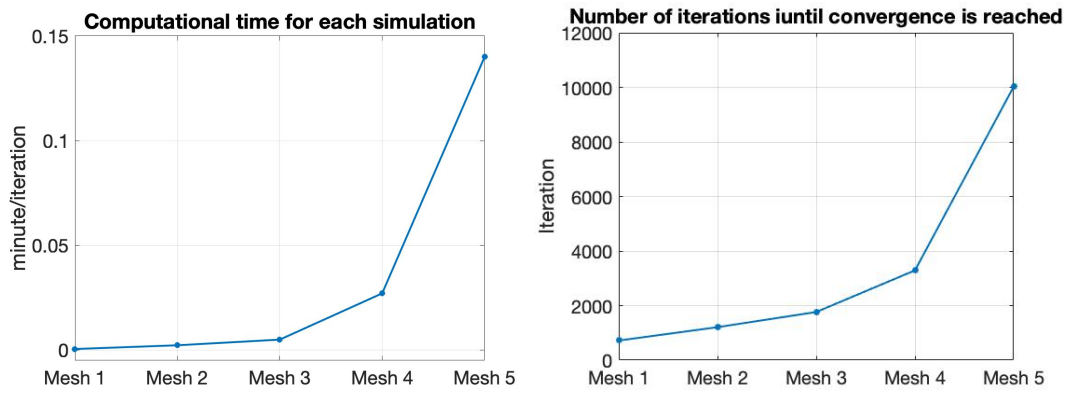

(a) Computational time

(b) Iterations until converged

Figure 5.15: The graph shows the computational time and the total number of iterations until convergence is reached for each mesh included in the sensitivity study.

The computational time and the number of iterations until convergence is reached differed significantly between the meshes, which can be seen in Fig. 5.15. Here, the computational time per iteration was determined by calculating the number of iterations performed in one minute and convergence is said to be reached when the residuals change less than 1 %.

Mesh 3 capture the same overall behavior as Mesh 5, see Fig. 5.11-5.14. It yields values that deviate by 0.4-6 % from Mesh 5 (except the bottom wall shear stress for the confetti at 90°, that deviates with 50 %). Even though Mesh 4 delivers results in the same range as Mesh 3, Mesh 3 is 247 % faster than Mesh 4, and 2760 % faster than Mesh 5. Mesh 2 is 50 % faster than Mesh 3, however, it deviates with 1-8 % from the values obtained from Mesh 5, thus is not as accurate as Mesh 3.

Considering this, Mesh 3 seems to be the optimal option, it saves computational time without losing too much accuracy. Since only the overall behavior of the confetti is of interest, this small loss in accuracy due to a coarser mesh, is considered to be negligible.

The result of the mesh sensitivity analysis is considered applicable for the final case, as the main feature of the flow that is to be resolved occurs downstream of the confetti which is the same in both cases, since the diameter of the pipes and dimensions of the confetti are the same.

5.1.4 The Final Model

Now that the correct model of the behavior of the flow and the confetti, as well as the interaction between them, is achieved, the Final model can be finalized. The geometry of the pipe is changed to include a T-junction, in Abaqus/Standard. One confetti is set at each inlet, oriented horizontally and aligned with the center line of the pipe, as shown in Fig. 5.16.

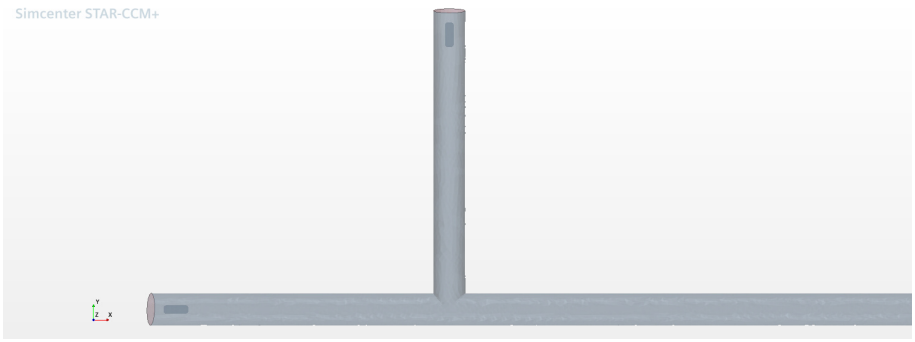

Figure 5.16: The Final model.

Geometry

The pipe diameter is consistently 45.2 mm throughout the pipe. The total length of it is 1.9 m and the junction is placed such that both shorter ends of the pipe are 0.4 m long, cf. Fig. 5.17. The dimensions of the confetti are as previously 35x12.1 mm. However, the thickness is set to 0.2675 mm, to match the thickness used in the physical tests. An overset region, inflated 2.5 mm in respect to the surface of the confetti in each direction, for both confetti is applied. The overset region is now bigger compared to the previous cases. Since the mesh used is coarser compared to the previous models, the overset region needs to be bigger to ensure enough active cells within the overset mesh. Too few active cells can cause unrealistic deformation of the confetti as a result of inadequately resolution of the flow parameters, such as the pressure, near the confetti.

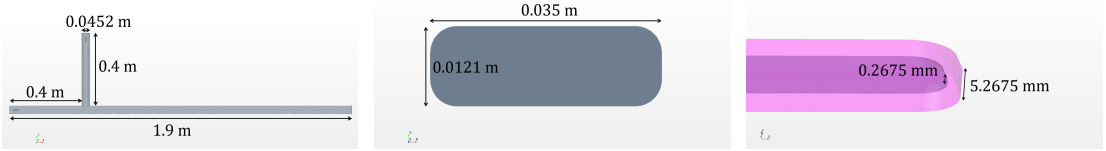

(a) The T-junction pipe (b) The confetti (c) The overset

Figure 5.17: The dimensions of the domain used in the Final model.

Material

The fluid flow is modeled as air, using an ideal gas approximation with isothermal conditions. Due to the high Re-number, the k-ϵ model is applied to model the turbulence.

The confetti are modeled using an anisotropic elasto-plastic material, using Hill's yield criterion with isotropic hardening. The constitutive material model presented in Section 2 assumes orthotropic material behavior. However, to fully capture the anisotropic behavior of paperboard, the yield stress ratios R_{ij} are altered in Abaqus/Standard, allowing different material behavior in the in-plane material directions. This constitutive material model is used, due to its accuracy. Physical tensile tests performed by [15], show that this material model coincides well with the data provided by the tests, cf. Fig. 5.18.

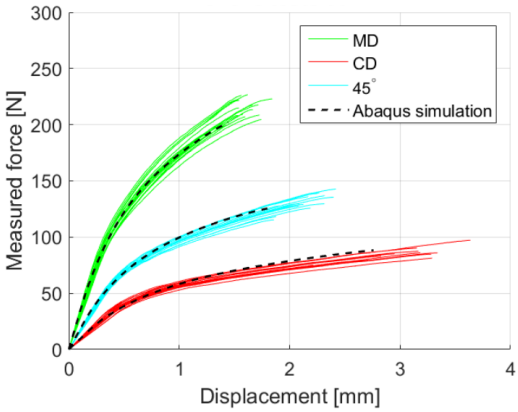

Figure 5.18: The validation of the constitutive model, provided by tensile tests on paperboard. Here, the green, blue and red curves represent the tensile tests in the three different material directions and the dashed line is the constitutive material model [15].

To save some computational time, the plasticity of the constitutive material model is omitted. Since no plastic deformation is expected, it is assumed that the results obtained are still close enough to reality. However, for comparison, one case was run with the plasticity included.

Mesh

The fluid and the overset region for the confetti are meshed using the automated mesh controls provided by STAR-CCM+. With a base cell size for the mesh elements of 0.6 mm (in accordance with the mesh sensitivity analysis) the confetti and pipe are meshed. The mesh for the confetti can be seen in Fig. 5.19. The same cell size is adopted in the entire domain, except for the prism cells, to ensure accurate interpolation between the background mesh and the overset mesh. Prism cells are applied around the confetti, to properly resolve the pressure and wall shear stress at the confetti surface. Five layers of prism cells, with a 1.5 prism layer stretching are used, see Fig. 5.20a-b. In order to resolve the near wall effects and the viscous sublayer, prism cells, using the same technique as for the confetti, are introduced along the pipe wall, see Fig. 5.20c-d. This resulted in a final cell count of the pipe of 21 000 000 cells and 30 000 for the confetti, including the overset mesh. The function "All Y+ Wall Treatment" is invoked, to ensure a good resolution of the flow in the boundary layer.

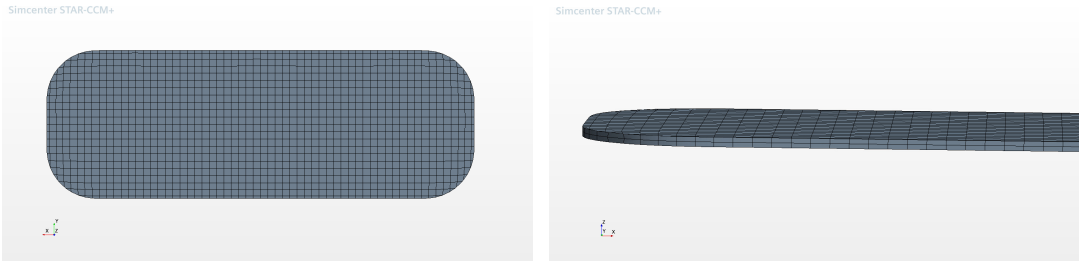

(a) Confetti, top view (b) Confetti, side view

Figure 5.19: The mesh in STAR-CCM+ of the confetti. The same mesh conditions are applied to both meshes, thus only one of the confetti is displayed.

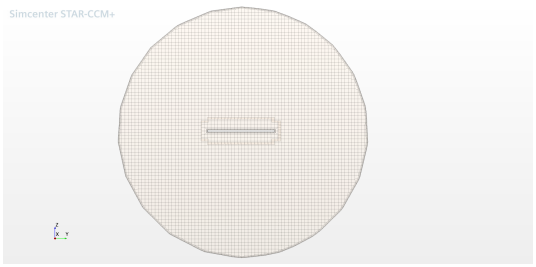

(a) Circular cross-section of pipe with confetti and overset.

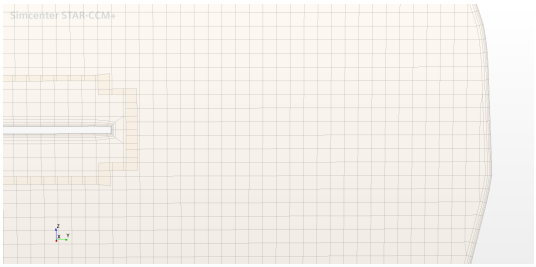

(b) Circular cross-section of pipe with confetti and overset, zoomed in.

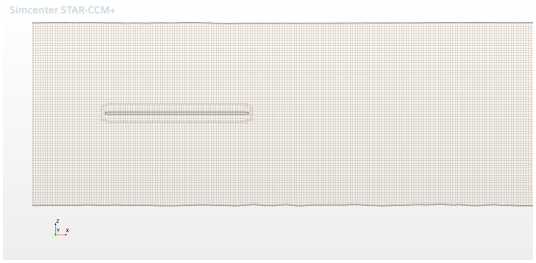

(c) Cross-section of pipe and confetti

(d) Prism layers along wall

Figure 5.20: The mesh in STAR-CCM+ of the T-junction pipe.

In Abaqus/Standard, solid, 8-node elements of the type C3D8I are used to mesh the confetti. Modeling contact between bodies is easier using solid elements, rather than shell elements, since these only occupy a theoretical space. Thus, solid elements are chosen to discretize the confetti, see Fig. 5.21a-b.

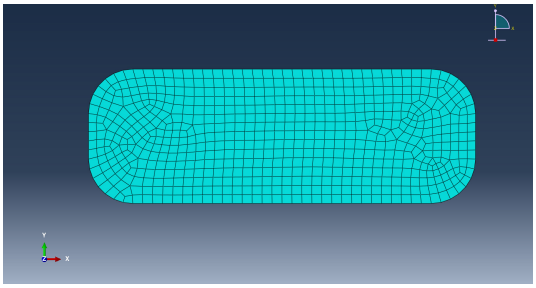

(a) The confetti

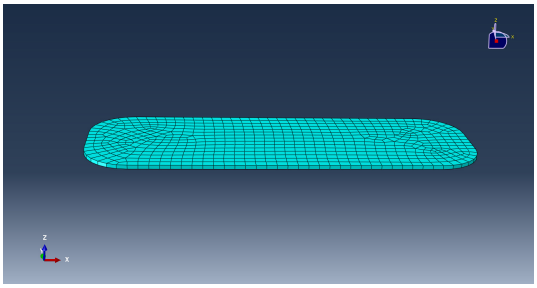

(b) The confetti, side view

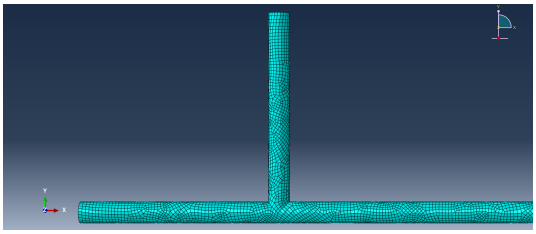

(c) The T-junction pipe

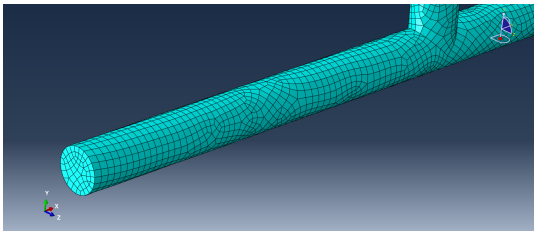

(d) The T-junction pipe

Figure 5.21: The mesh in Abaqus/Standard.

Due to the small thickness of the confetti, only one layer of elements is required to completely model its volume. This puts harder requirements on the accuracy of the elements.

Hence, C3D8I elements are used, since they employ full integration and incorporate incompatible modes, they ensure good accuracy when computing the displacement of the nodes, as mentioned in Section 2. The pipe is meshed using both quadrilateral and triangular facet cells, of the types R3D3 and R3D4, see Fig 5.21c-d. Since the pipe does not move, it is modeled using a discrete mesh with these rigid body elements, to save computational power. The final cell count for the pipe is 8500 and 600 for each confetti.

Boundary and initial conditions

Initially the confetti are non-deformed and placed in each inlet of the pipe. The inlet velocity is set to 5.1 m/s at the inlet to the straight pipe and 5.3 m/s at inlet to the upper pipe, and a zero pressure outlet condition is imposed, see Fig. 5.22. These boundary conditions were set, even though suction conditions, resembling the flow conditions in a vacuum cleaner, apply to the pipe. It was tried to impose an outlet velocity and zero pressure inlets. However, this kind of set-up is ill-posed, thus unable to converge, it was decided to impose inlet velocities and a pressure outlet. All walls of the pipe, and the surfaces of the confetti, are set to no-slip conditions. As the simulations were performed, the first iterations were run using steady state conditions to obtain a fully developed flow. After 500 iterations transient conditions were re-applied and the co-simulation is started.

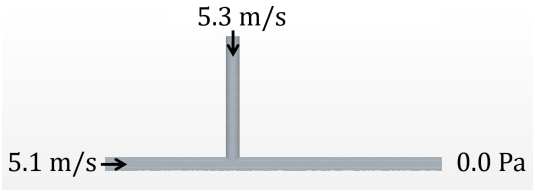

Figure 5.22: The boundary conditions applied in the Final model.

Surface-to-surface contact conditions are applied in Abaqus/Standard for all contacts between the three bodies. A soft contact, with a linear pressure-overclosure relation, is employed with the inclination constant set to $k = 1e9$. This kind of contact was chosen based on the contact analysis performed as the Two confetti model was developed.

In STAR-CCM+, a ZeroGap interface was chosen for all contact pairs with close proximity activated as in the Modified Model.

Solvers

To solve the governing equations of this FSI problem, Newtons method is employed for the structural part with a minimum step size of 1e-4 s. For the fluid part the segregated flow solver, using the SIMPLE algorithm, is applied with a constant time-step size of 1e-4 s, as set in Abaqus/Standard. In the previous models an adaptive time step was applied. However, the controls for the adaptive time-step differ between Abaqus/Standard and STAR-CCM+, resulting in a mismatch in the physical time during the simulation and ultimately caused the simulations to crash. It was tried to control this procedure, but all attempts failed. Thus, the adaptive time-step was omitted, and a constant time-step was set. The total maximum physical time is set to 5.0 s.

To ensure convergence and a numerical stable solver, the pressure and the turbulent viscosity are under-relaxed. The under-relaxation parameter for the pressure was changed

from 0.2 to 0.1, and from 1.0 to 0.6 for the turbulent viscosity.

The simulation was run on 224 processors in parallel and the resulting average computational time for the simulation is computed to be 0.034 minutes per iteration. In total, this simulation took 5 days to complete.

5.2 Experimental set-up

To be able to validate the simulation results, physical experiments are conducted. Using a transparent PVC pipe, with the same size as used in the set-up of the simulations, connected to a vacuum cleaner the simulations could be reenacted. Images of the complete set-up can be seen in Fig. 5.23. The videos are mainly shot from above, providing a good view of how the confetti are transported through the pipe. However, some videos are also shot from the side, to create footage to see how the confetti are affected by gravity.

Figure 5.23: The set-up used for the experiments.

The vacuum cleaner is mounted onto the pipe and secured with duct tape. Using an anemometer, the correct vacuum setting, that gives 5 m/s for the air flow velocity at both inlets of the pipe, is established. The anemometer used, is a Testo 416, which is a measuring device for measuring flow speeds by means of a low-friction telescopic impeller. A dark blue backdrop is used to provide a good contrast to the white confetti and LED light heads, mounted on telescope arms, ensure good lighting for the high-speed camera. To reduce light reflections due to the glossy surface of the pipe, the LED lights are covered with parchment paper, resulting in a more diffuse lighting.

The high-speed camera used is an Olypmus i-SPEED 3 with 1000 fps and a resolution of 1280x1024. The confetti are hold by hand, centered in each opening of the pipe, and released simultaneously. To ensure the same material behavior as in the simulation model, confetti produced in the test plant at Tetra Pak® are used.

Chapter 6

Results and discussion

A total of 18 experiments were conducted, where 14 are filmed using a top view, i.e. the complete T-junction is visible, and 4 were filmed using a side view, where only the first part of the straight pipe is visible from the side, cf. Fig. 6.1. Out of the 14 experiments filmed from a top view, 3 collisions of the two confetti were captured. The top view was used to observe the trajectories of and the interaction between the two confetti, while the side view was employed to assess the influence of the gravity and initial position of the confetti.

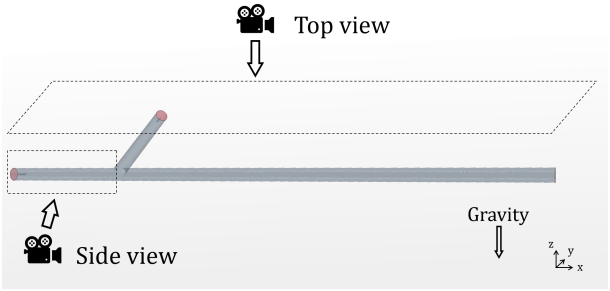

Figure 6.1: Camera angels used during experiments.

Since two different camera angles were employed during the experiments, all simulations are observed from the same two angles. In total, five simulations were run on the T-junction case: four cases with the confetti at different initial inclinations (without plasticity included in the material model) and a fifth simulation, with the plasticity included. A compilation of the simulations conducted can be seen in Table 6.1. Simulations, with different initial inclinations of the confetti applied, were run to investigate what influence the initial position has on the trajectory and the evacuation speed of the confetti. A sketch of the initial positions of the confetti can be seen in Fig. 6.2.

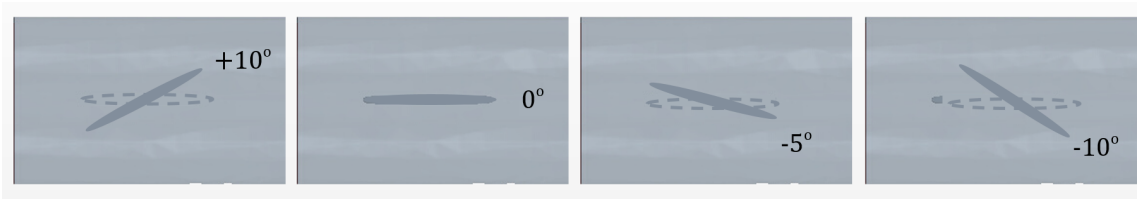

Figure 6.2: Sketch of the initial inclination of the confetti in the different simulations run.

Table 6.1: An overview of the numerical simulations conducted on the T-junction case.

Simulation case	Plasticity included	Inclination of confetti
1	No	+10°
2	No	0°
3	No	-5°
4	No	-10°
5	Yes	0°

Using image analysis, the centroid of the confetti are tracked, to be able to compare the trajectories of the confetti in the numerical simulations and the physical experiments. The software *Tracker* [16], which is a free and open source video analysis and modeling tool, is used since it offers manual tracking. Due to the reflections in the pipe in the videos and the high number of rotations in the movement pattern of the confetti, automatic tracking-software were not able to track the confetti in all frames. Therefore, the tracking is performed manually.

6.1 Side view

6.1.1 Numerical results

In Fig. 6.3 the full trajectory of the confetti with the initial inclination of -5° can be seen. Using the tracking tool, the centroid of the confetti is tracked. Employing a snapshot-function, several frames from the simulation are depicted in one image. It can be seen how the confetti moves through the pipe by bouncing against the walls in a rotating fashion.

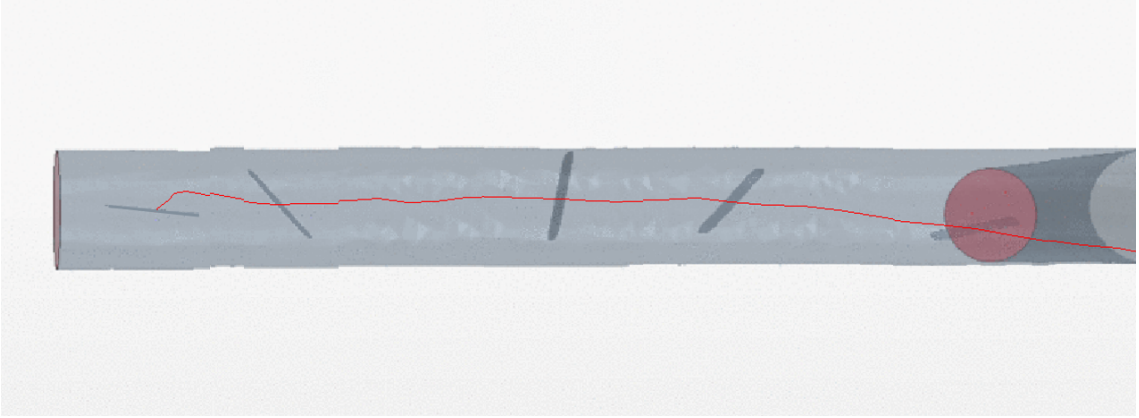

Figure 6.3: Trajectory of confetti in simulation with -5° initial inclination, side view.

In Fig. 6.4, the velocity distribution is depicted in a contour plot of a cutting plane. One can see how the flow is mainly affected downstream by the confetti. From the velocity distribution it can be noted that the bulk flow has a velocity of about 5 m/s and that it is zero along the walls, as expected. Downstream of the confetti, a wake is created, with recirculating flow.

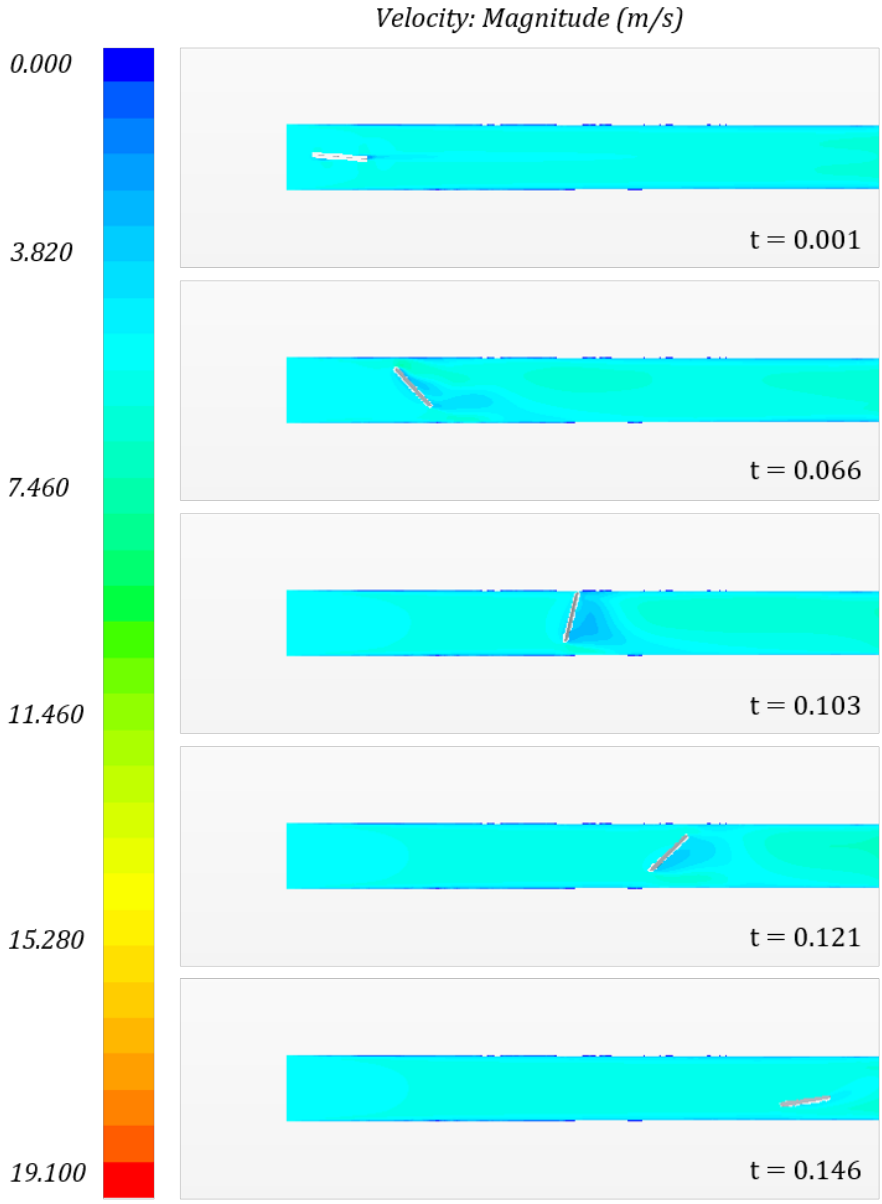

Figure 6.4: The velocity distribution, side view of the simulation case with -5°.

The trajectory data from all simulations are compiled in Fig. 6.5, where the trajectories and the x-coordinate as a function of time can be seen.

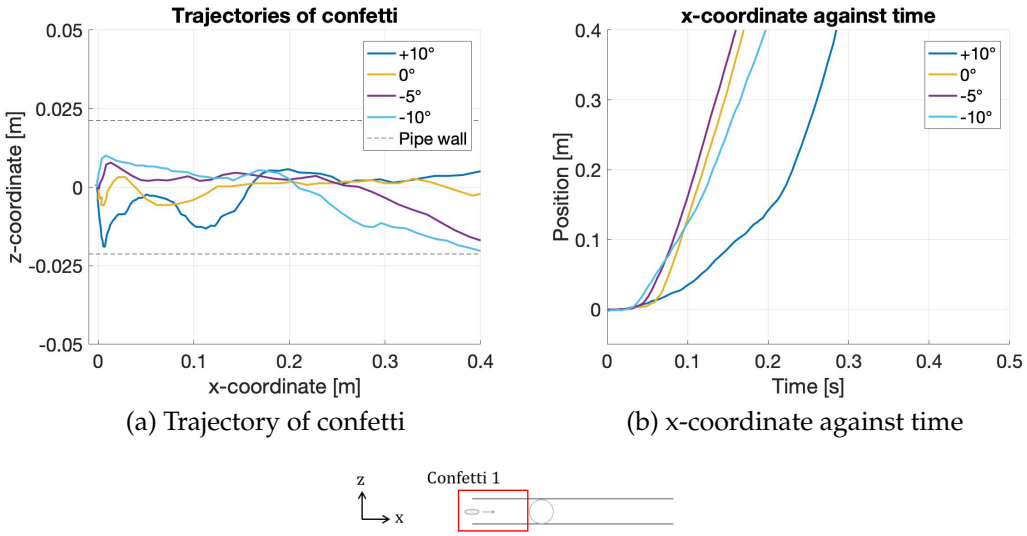

(a) Trajectory of confetti

(b) x-coordinate against time

Figure 6.5: All data from simulations, side view

Fig. 6.5 shows that the confetti with the initial angle of +10° is the slowest confetti to reach the end of the pipe. At the start, the confetti moves towards the bottom, where it loses kinetic energy partially due to the impact against the wall and partially due to the low velocity flow near the wall. In the other three simulations, the confetti seems to have similar speed through the pipe.

In Fig. 6.5a one can see that the confetti with zero or positive initial inclination have a tenancy to move downward, while the confetti with a negative initial inclination angle move upward. This behavior is due to the pressure and velocity distribution on the top and bottom of the confetti.

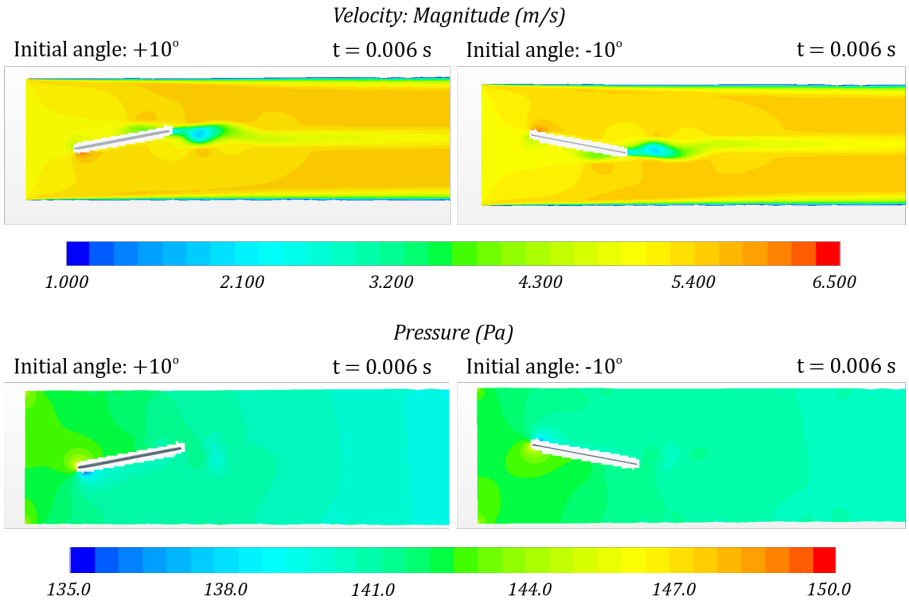

Figure 6.6: Initial velocity and pressure distribution around confetti, with the initial inclination angles -10° and +10° compared.

As pictured in Fig. 6.6, it can be observed that the confetti inclined +10° has a lower velocity on the top surface compared to the bottom surface. This implies that the pressure is higher on the top surface, compared to the bottom surface as seen in Fig. 6.6, thus forcing the confetti downward. The opposite behavior applies to the confetti with the negative initial inclination.

The initial inclination of the confetti governs its initial movement, and thus the final evacuation time. From these simulations it can be seen that a positive initial inclination is not preferable, cf. Fig. 6.5b, since it increases the risk of the confetti getting stuck at the wall. With a negative inclination angle, the confetti moves upward and due to gravity, the risk is lower that the confetti will get stuck in the low speed flow near the wall and loose kinetic energy. However, this might be too little data to make statistically accurate conclusions applying generally to the behavior of all confetti.

6.1.2 Experimental results

In Fig. 6.7 the full trajectory of the confetti can be seen. Using the tracking tool, the centroid of the confetti is tracked. One can see how the confetti moves through the pipe by bouncing against the walls and rotating around its own axes.

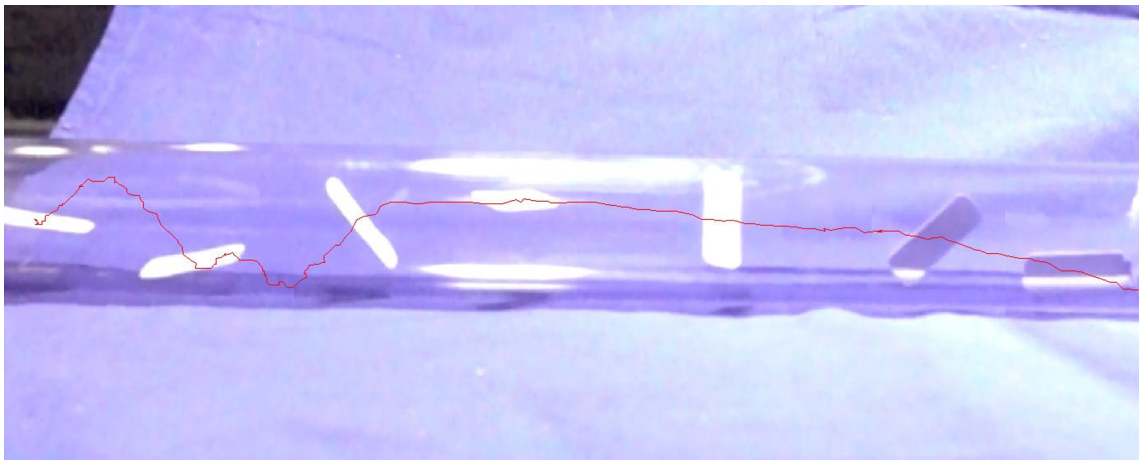

Figure 6.7: Snapshots from experiment, side view.

The trajectories of the confetti, for all videos from the experiments using the side view, can be seen in Fig. 6.8a and the x-coordinate of the confetti, as a function time, is depicted in Fig. 6.8b. Note that due to a slightly tilted frame while filming the experiments, the pipe wall in Fig. 6.8a appears to be tilted as well. The pipe used has a constant diameter throughout.

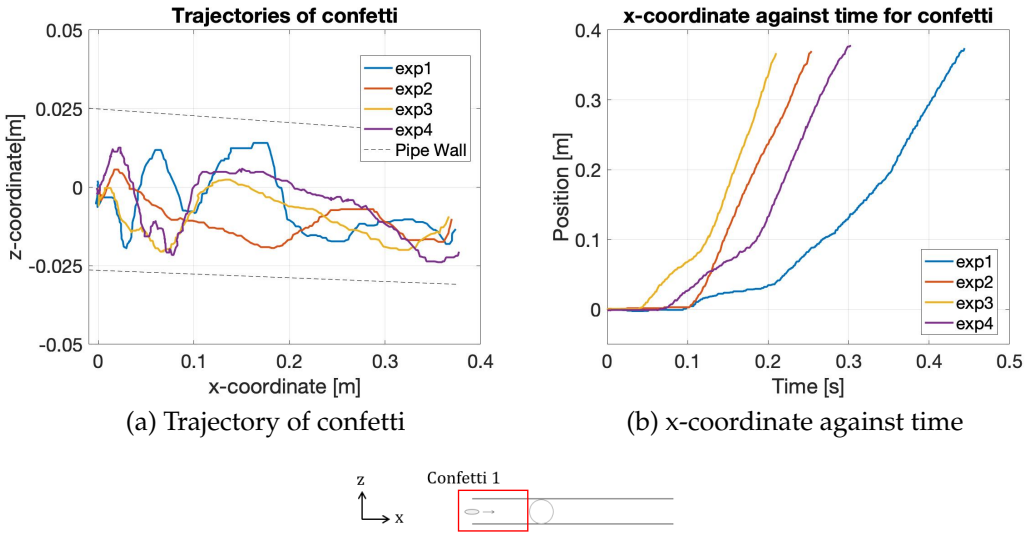

(a) Trajectory of confetti

(b) x-coordinate against time

Figure 6.8: All data from experiments, side view

From Fig. 6.8b one can see that the confetti in Experiment 1 is considerably slower than the confetti in the other experiments. At the start, this confetti bounces against the bottom wall of the pipe, lying flat against the surface. Since, the flow is slower along the wall of the pipe, as observed in the velocity contour plot in Fig. 6.4, the confetti loses a considerably amount of kinetic energy, thus slowing down. A similar behavior can be observed for the confetti in Experiment 4. This confetti initially moves upward, and is caught by the low speed flow near the wall. However, due to gravity it is picked up by the main flow considerably faster than the confetti in Experiment 1.

6.1.3 Comparison

In Fig. 6.9a and 6.9b the trajectories and the x-coordinate against time, from the experiments and FSI-simulations, for the side view are compared.

Looking further at Fig. 6.9a, one can clearly see the stochastic behavior of the confetti. The strong dependence of the initial conditions plays a large role, especially in the physical experiments, making it hard to draw some kind of conclusion regarding the general behavior of the trajectory. For this, more physical experiments would be required.

Comparing the evacuation speed of the confetti in the simulations with the physical experiments one can generally say that the evacuation speed is faster in the simulations than in the experiments, cf. Fig. 6.9b. In both the simulation and the experiments, one confetti dropped to the bottom of the pipe and lost some kinetic energy, thus slowing down. Also this course of events is faster in the simulations compared to the physical experiments. This could, however, be the cause of the naturally stochastic behavior of the trajectory of the confetti.

Using linear interpolation, the absolute value of the x-component of the velocity is calculated and displayed in Fig. 6.9c. The absolute velocity of the confetti calculated from the individual experiments and simulations are compared. The average value is calculated using the velocities measured from the experiments only.

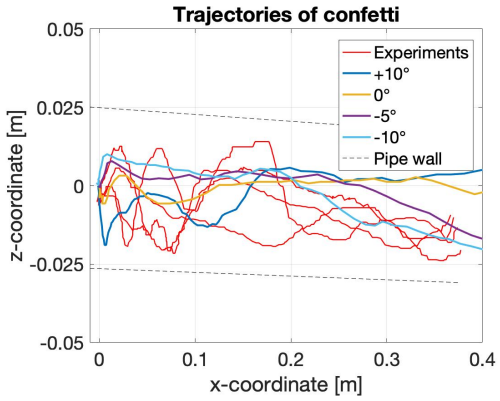

(a) Trajectory of confetti

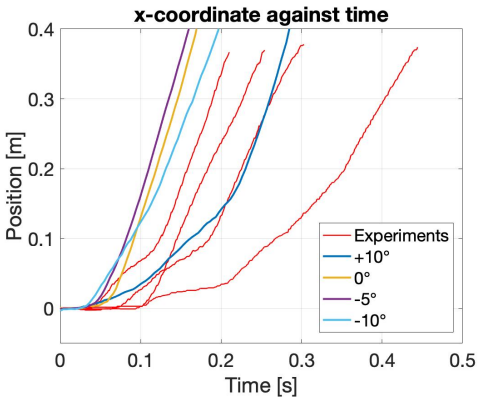

(b) x-coordinate against time

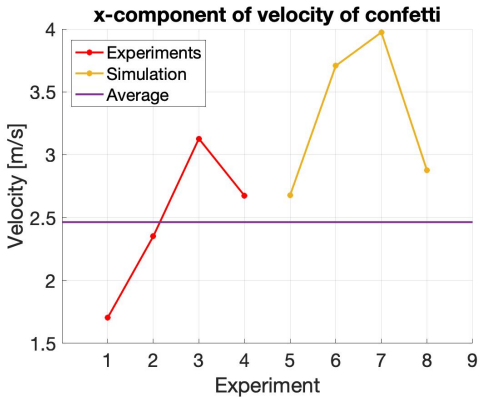

(c) Absolute velocity, x-direction

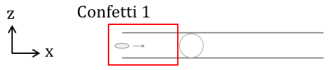

Figure 6.9: All data from simulations and experiments compared, side view. The average is calculated using the experimental values only.

Here, it is confirmed, that the simulations generally predict a higher evacuation speed. This could be the result of losses, that the confetti experiences in the physical experiments, that are not captured by the simulations. These kinds of losses could possibly be due to a slight static electrical charge on the PVC-pipe, used in the experiment, which could have a decelerating effect on the confetti. However, the differences could also be the result of different release times of the confetti or due to different flow velocities inside the pipe due to fluctuations in the pressure exerted by the vacuum cleaner.

6.2 Top view

6.2.1 Numerical results

In Fig. 6.10 the velocity distribution can be seen for key time stamps from the simulation. The main flow has a velocity of about 5 m/s in the smaller branches of the pipe and 13 m/s in the long part of the pipe. A recirculation area is located just downstream of the junction, bordered by a high velocity part of the flow.

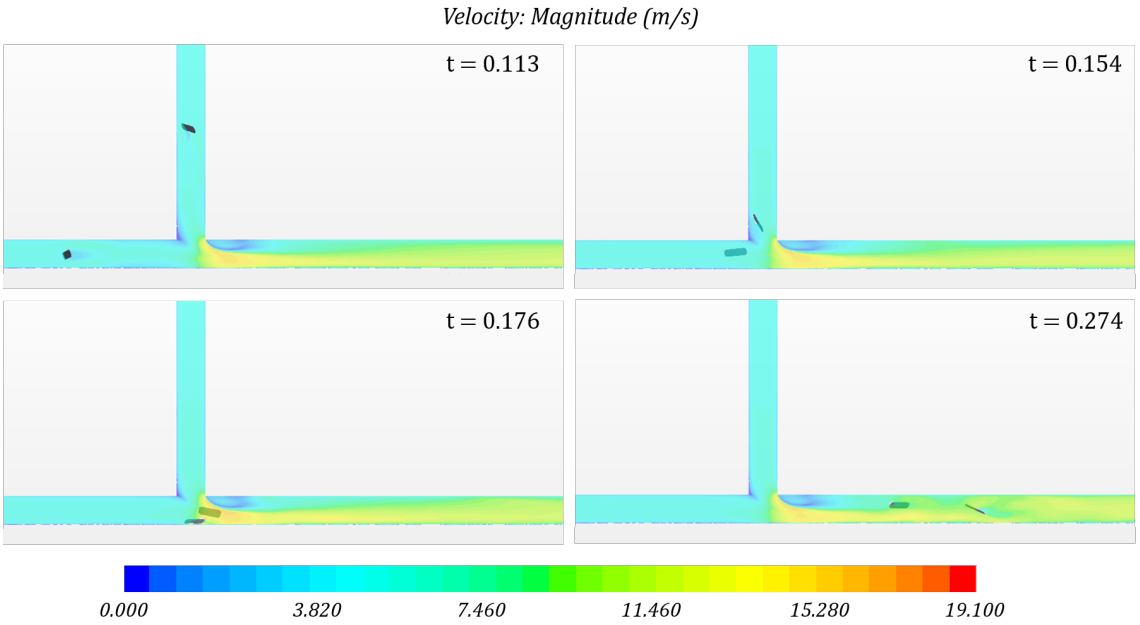

Figure 6.10: The velocity distribution, top view of the simulation case with -5°.

The trajectories, displaying the full movement of both confetti are depicted in Fig. 6.11. Here, the red and green line represent Confetti 1, coming from the left, and Confetti 2, coming from the top, respectively.

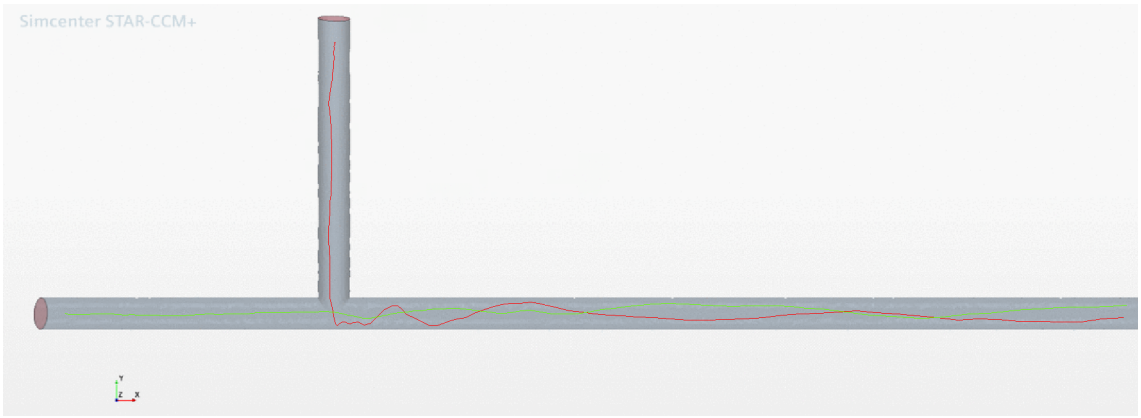

Figure 6.11: Trajectory of both confetti in simulation, top view.

All trajectory data, obtained from the simulations, are compiled in Fig. 6.12, where the trajectories of both confetti can be seen.

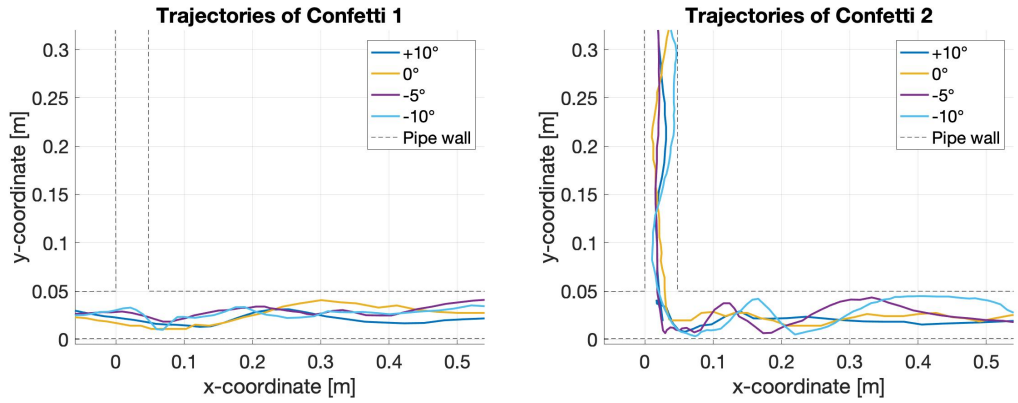

(a) Trajectory of Confetti 1 (b) Trajectory of Confetti 2

Figure 6.12: The trajectories of the two confetti in all simulations, top view.

As for Confetti 1, cf. Fig. 6.12a, it seems to follow a similar path, regardless of initial inclination. It can clearly be seen how they are guided around the recirculation area, by the high speed flow, downstream of the junction, at about 0.05-0.15 m on the x-axis. The same applies for Confetti 2, coming from the top, cf. Fig. 6.12b. After passing the junction, the confetti hits the bottom wall, bounces and is picked up by the bulk flow. It can be noted that in all simulation cases Confetti 2 seems to cross the same point, at y = 0.14, despite the stochastic behavior of the trajectory.

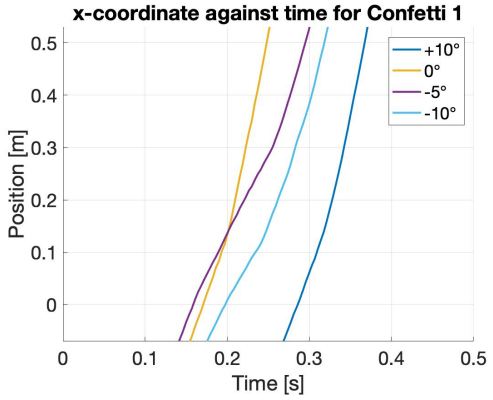

(a) x-coordinate against time, Confetti 1

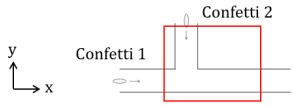

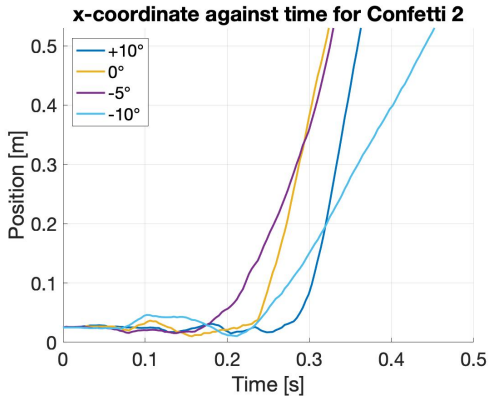

(b) x-coordinate against time, Confetti 2

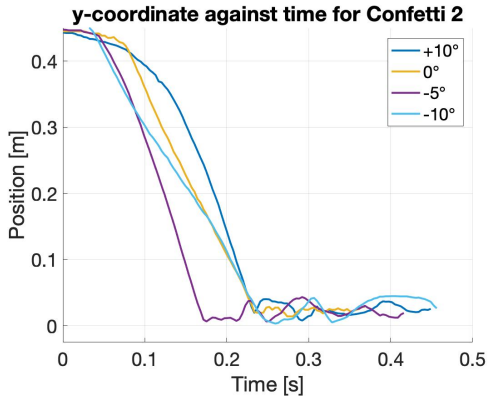

(c) y-coordinate against time, Confetti 2

Figure 6.13: The position against time for the two confetti in all simulations, top view.

The trajectory data, against time, is to be seen in Fig. 6.13. It can be noted that the slope of the curves in the plot of Fig. 6.13a increases for larger values of x, indicating that the evacuation speed of Confetti 1 increases as it moves through the pipe. Despite bouncing against the walls, the velocity increases, mainly due to the higher velocity bulk flow in the long part of the straight pipe. A similar behavior can be noted for Confetti 2, cf. Fig. 6.13c, displaying the position against time when still in the upper pipe. The inclination of the curves, increases as time increases, indicating acceleration. As observed previously, the confetti starting at +10°, is the slowest one. For the second part of the curves, only small variation can be seen due to the limited space of movement in the y-direction in the part of the pipe after the junction.

In Fig. 6.13b the x-coordinate as a function of time for Confetti 2 is depicted. For the first part, only small changes are observed, due to the limited space for movement in x-direction in the upper branch. As Confetti 2 moves past the junction, an increase of x-position is seen. Since the confetti has covered quite a large distance at this point, the different evacuation velocities are merely an effect due to its movement pattern, rather than its initial inclination angle.

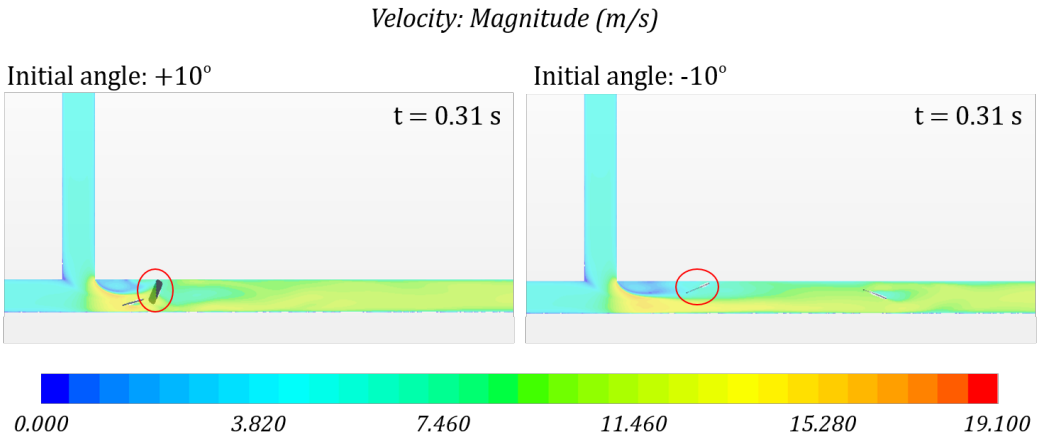

Figure 6.14: The orientation of confetti after passing junction. Confetti 2, coming from the top, is marked with a red circle. The contour plot shows the velocity distribution.

After passing the junction, Confetti 2 ends up with different orientations, thus exposing itself to the flow with different cross-sectional areas, resulting in different evacuation velocities. Fig. 6.14 shows the orientation of the two confetti for the cases +10° and -10°, shortly after having passed the junction. Confetti 2 is here marked with a red circle. One can see that Confetti 2, in the first case faces the flow with a larger cross-sectional area, compared to the -10° case, where the confetti is oriented in a vertical fashion, in a low-velocity flow area. Thus, the confetti loses speed while the confetti in the +10° case gains a higher speed, as seen in Fig. 6.13b.

6.2.2 Experimental results

Snapshots from the physical experiments, using the top view, are depicted in Fig. 6.15. It can be seen how the two confetti come from each direction, collide at the junction, and exit the pipe. The confetti travel through the pipe, in a rotating and bouncing manner.

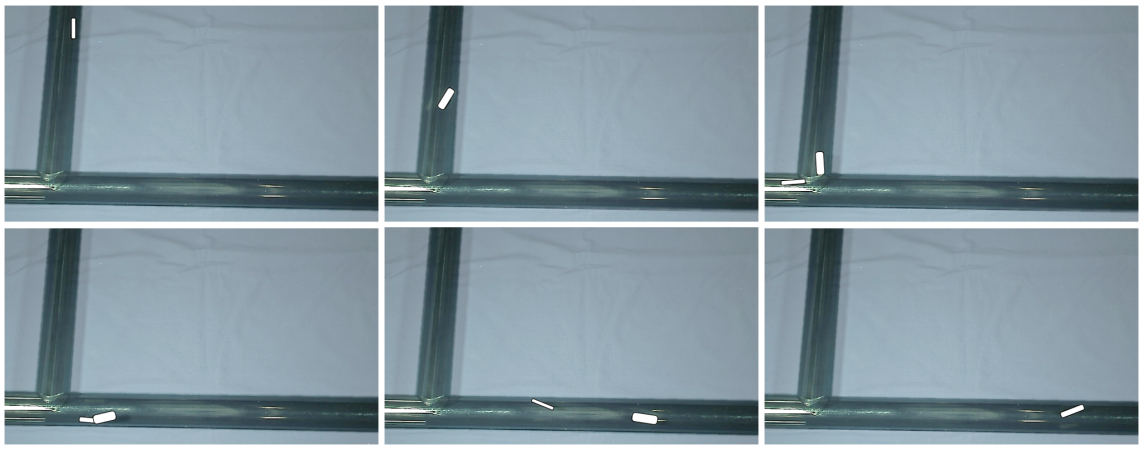

Figure 6.15: Snapshots from experiment, top view.

In Fig. 6.16 the trajectories of the two confetti can be seen. The green and red line represent Confetti 1 coming from the left and Confetti 2 coming from the top, respectively.

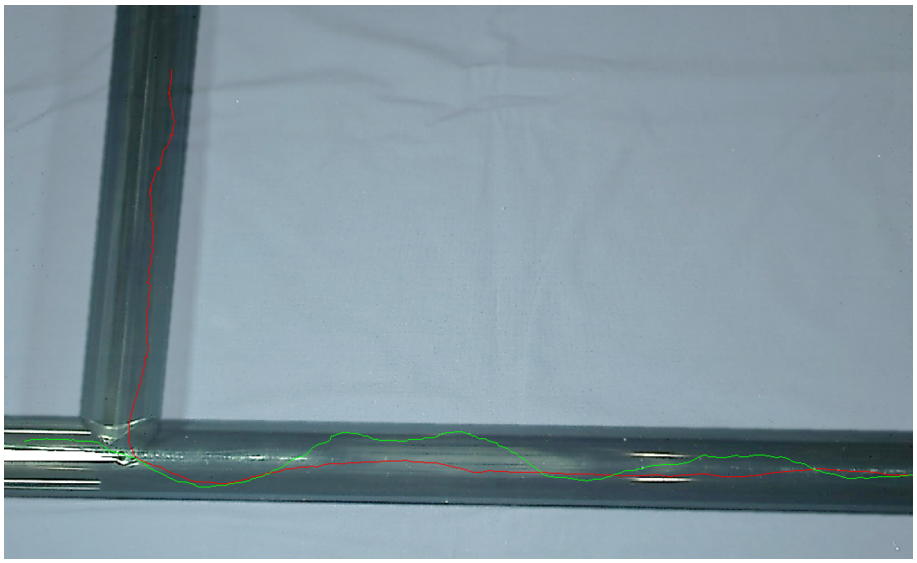

Figure 6.16: Trajectory of both confetti in experiment, top view.

The trajectories for both confetti from all experiments are compiled in Fig. 6.17, where once again Confetti 1, entering from the left, is marked with green and Confetti 2, coming from the top, is marked with red. Due to a slightly tilted frame in the videos from the experiments, the pipe wall in the graphs of Fig. 6.17 appears to be tilted, however, the pipe diameter is constant throughout.

As observed in the side view cases, the confetti covers quite a large range of the pipe diameter due to its random behavior. In spite of this, it can be noted how Confetti 1 is guided by the flow, around the recirculation area after the junction, cf. Fig. 6.17a. In most experiments, Confetti 1 avoids the recirculation area due to the adjacent high speed flow, bounces against the top wall, and enters the bulk flow where its movement becomes random again. For Confetti 2, a similar behavior can be seen, Fig. 6.17b. After exiting the upper pipe, it bounces against the bottom wall of the straight pipe and, governed by the high speed flow adjacent to the recirculation area, it hits the top wall. The guidance by the high speed flow adjacent to the recirculation area, is especially visible in Fig. 6.17c.

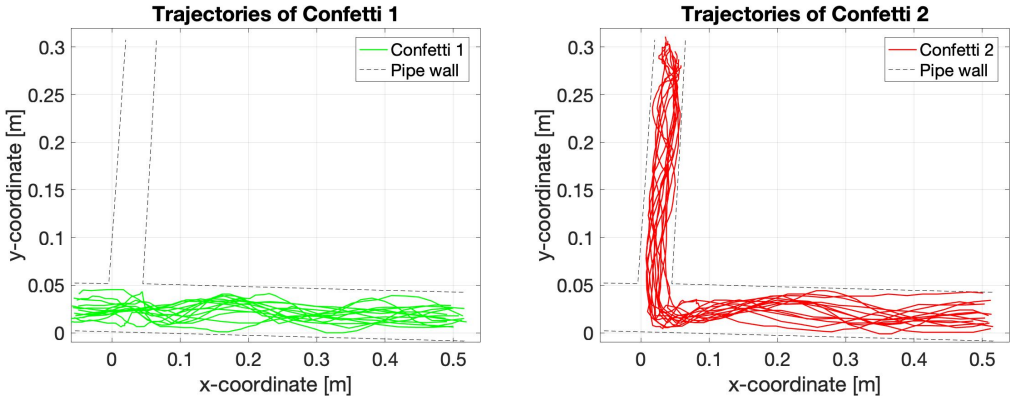

(a) Trajectory of Confetti 1

(b) Trajectory of Confetti 2

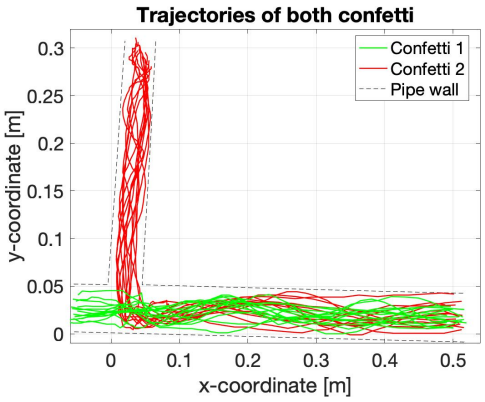

(c) Trajectory of both confetti

Figure 6.17: The trajectories of the two confetti in all experiments, top view.

In Fig. 6.18 the x- and y-coordinate as a function of time for both confetti are depicted. The three lines marked with a blue color represent the experiments where the confetti collided in the T-junction. It should be noted that the large range of exiting times it most definitely a result of different release times of the confetti, due to the human factor. Thus, it should not be focused on the absolute times rather than the slope of the curves since these are comparable in respect to the absolute values of the time.

Similarly to the numerical result, we see the same overall behavior. In Fig. 6.18a the inclination of the curves becomes steeper as the time increases. The T-junction is located at about x = 0.05, thus, for some of the curves a bump can be observed here. In some cases, the junction causes an altered behavior of the confetti due to an impact with the wall or with the other confetti. In one of the cases with collision, a great deceleration of the velocity can be seen.

Albeit one might expect the confetti to loose kinetic energy due to bouncing, Confetti 2 proves the opposite when exiting the upper pipe, cf. Fig. 6.18b. For most cases, Confetti 2 gains speed which it can keep throughout the rest of the pipe. Only in a few cases, a deceleration can be observed at the junction, see the two curves to the right in the plot of Fig. 6.18b. Confetti 2 is not slowed down by the junction most definitely due to it entering a 13 m/s flow downstream of the junction, in respect to the 5 m/s flow where it started from. This helps it gaining kinetic energy and recover from the impact to the wall.

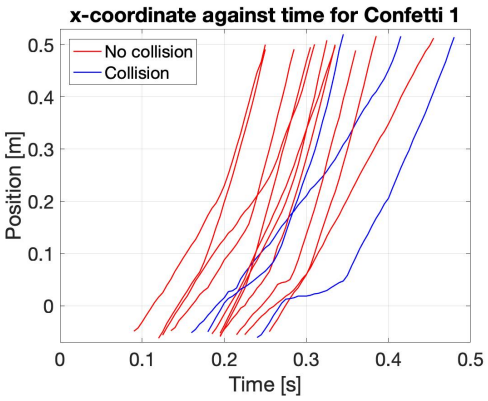

(a) x-coordinate against time, Confetti 1

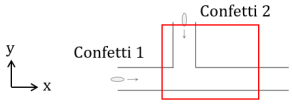

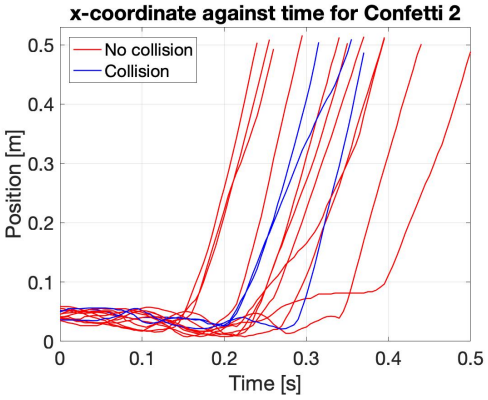

(b) x-coordinate against time, Confetti 2

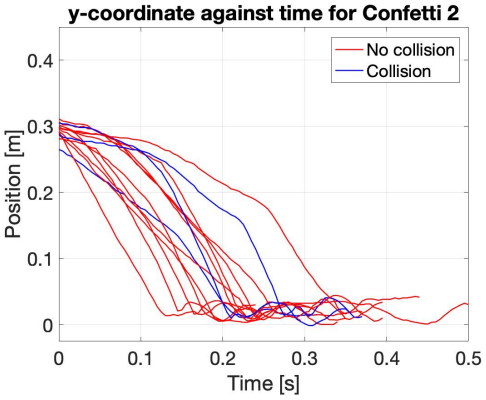

(c) y-coordinate against time, Confetti 2

Figure 6.18: The position against time for the two confetti in all experiments, top view. The three lines marked with blue, represent those cases where the confetti collided.

The same kind of behavior can be seen when observing the y-coordinate for Confetti 2. In Fig. 6.18c, one can see, that in especially two of the cases that the velocity of the confetti increases after having passed about half of the pipe. In these cases, the confetti bounces against the wall, thus changing orientation and suddenly exposing itself to the flow with a larger area, hence gaining speed.

6.2.3 Comparison

In Fig. 6.19 the trajectories from the experiments and simulations, using the top view are compared. The simulation results coincide well with the experiments, in the sense that the trajectories follow the same statistical pattern.

A comparison of the time dependence of the position of the confetti, confirm that the simulations capture the behavior of and interaction between the confetti well, see Fig. 6.20. Regarding the x-position of Confetti 1, Fig. 6.20a, similar slopes of the curves can be observed between simulation and experimental results. However, none of the simulation cases show a bump in the curve at the T-junction. This behavior might be captured if more simulations would be performed.

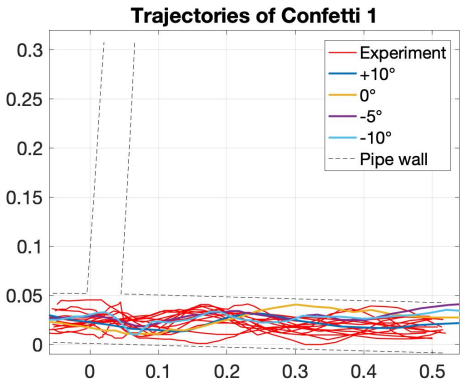

(a) Trajectory of Confetti 1

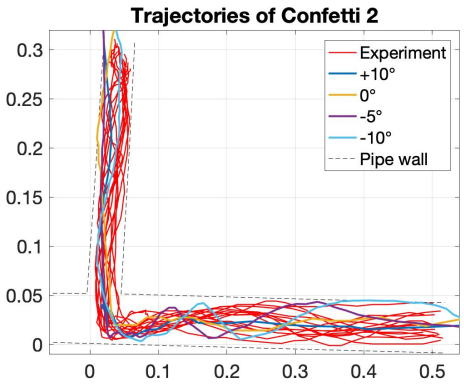

(b) Trajectory of Confetti 2

Figure 6.19: The trajectories of the two confetti in all simulations and experiments compared, top view.

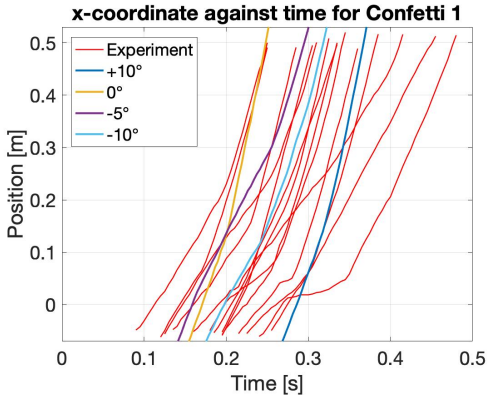

(a) x-coordinate against time, Confetti 1

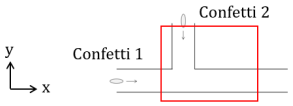

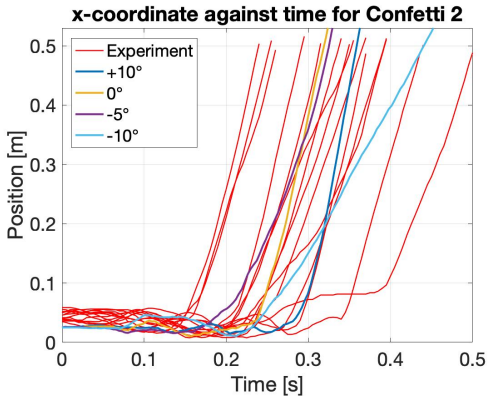

(b) x-coordinate against time, Confetti 2

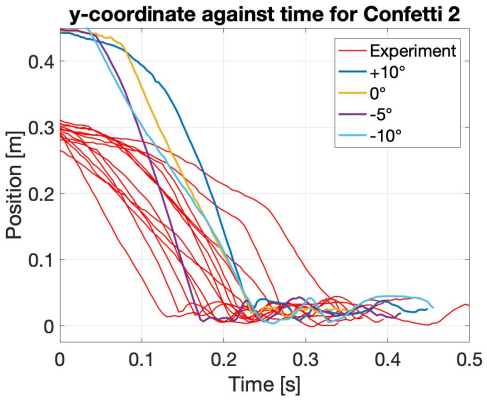

(c) y-coordinate against time, Confetti 2

Figure 6.20: The position against time for the two confetti in all simulations and experiments compared, top view.

The same applies regarding the x-coordinate of Confetti 2, see Fig. 6.20b. As for the y-coordinate for Confetti 2, the offset at the y-axis is due to different frame sizes of the images processed. In the videos from the experiments, a quite limited view of the pipe is provided due to a restricting angle of view in the camera lens used, while the full pipe can be observed in the simulations.

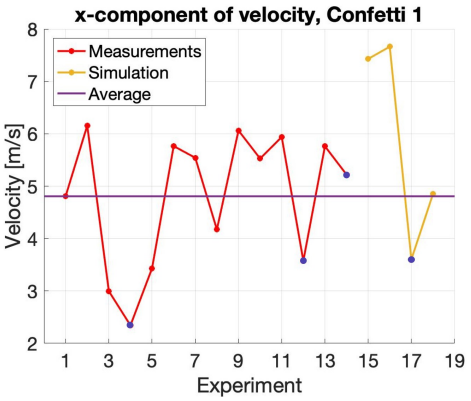

(a) Velocity, x-direction for Confetti 1

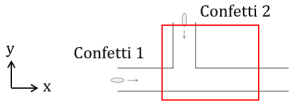

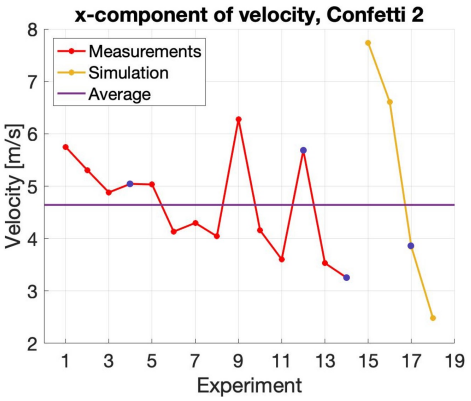

(b) Velocity, x-direction for Confetti 2

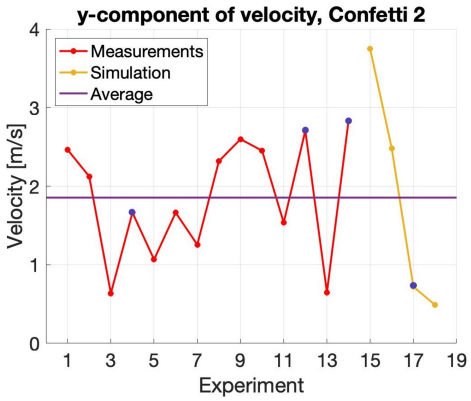

(c) Velocity, y-direction for Confetti 2

Figure 6.21: The absolute velocities of the two confetti in all simulations, top view. Data points marked with a blue dot represent cases where the confetti collided at the T-junction. The average is calculated using the experimental values only.

As for the side view, linear interpolation is used once again to obtain the absolute value of the x- and y-component of the velocity, which can be seen in Fig. 6.21. Data points marked with a blue dot represent the cases where the two confetti collided at the T-junction. Here, the absolute velocity of both confetti, calculated from the individual experiments and simulations, are compared. The average value is calculated using the velocities measured from the experiments only. Yet again, we see a quite large range of velocities and that the simulations are deviating more than expected. The cases where the confetti collided, are not the ones with the lowest velocity, indicating that the collision between the confetti does not affect them as expected. The average values in all cases apply mainly to the part of the pipe after the junction, where the bulk flow velocity is 13 m/s, however, the x-velocity for both confetti are in the range of 4-6 m/s, cf. Fig. 6.21a and 6.21b. At this point the confetti have traveled about 0.2-0.4 m in the pipe, after the junction, which might be too little to accelerate to higher velocities. In comparison, Confetti 2, while remaining in the upper part of the pipe, has a velocity in the range 1-3 m/s compared to the bulk flow velocity of 5 m/s, which is not as a large difference as after the junction, see Fig. 6.21c. From this one can conclude that the junction does slow the confetti down, and that a longer pipe is needed for the confetti to accelerate properly and reach higher velocities. However, a longer pipe could also increase the risk of a bad collision with the wall, thus resulting in the confetti getting stuck in the low velocity flow near the wall.

6.3 Plasticity vs pure Elasticity

In Fig. 6.22-6.24 the results from the material sensitivity analysis is depicted. The simulation where the confetti is modeled using an elasto-plastic material model (called *with plasticity*) is compared to the case where the confetti is modeled with a purely elastic material model (called *pure elasticity*). Both cases have the same boundary and initial conditions, and the confetti have the same initial positions with an inclination angle of 0°, with only the material model differing.

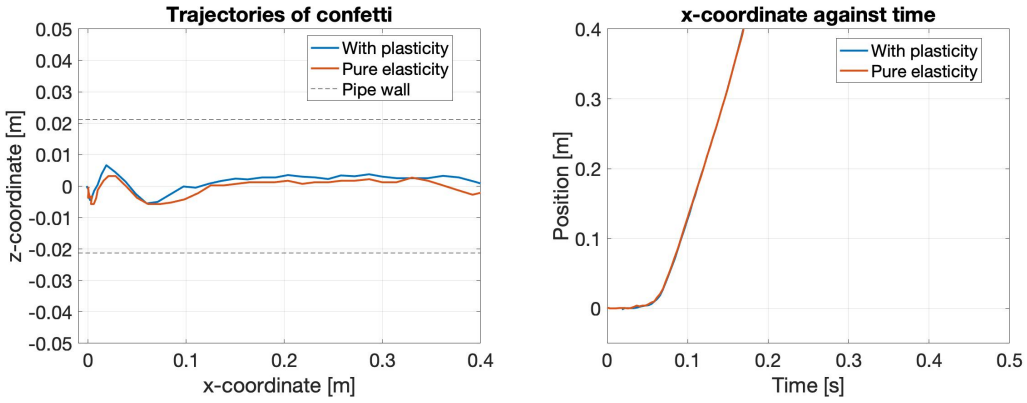

(a) Trajectory of confetti (b) x-coordinate against time

Figure 6.22: Plasticity vs pure elasticity, side view.

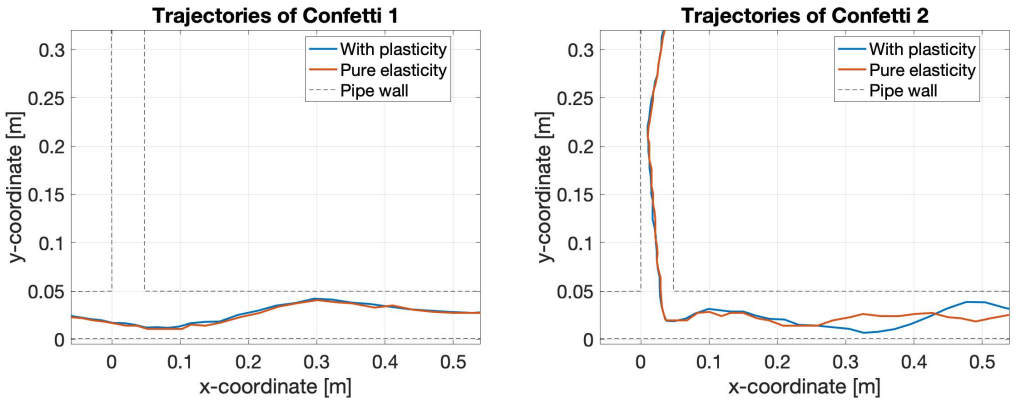

(a) Trajectory of Confetti 1 (b) Trajectory of Confetti 2

Figure 6.23: The trajectories of the two confetti comparing plasticity and pure elasticity, top view.

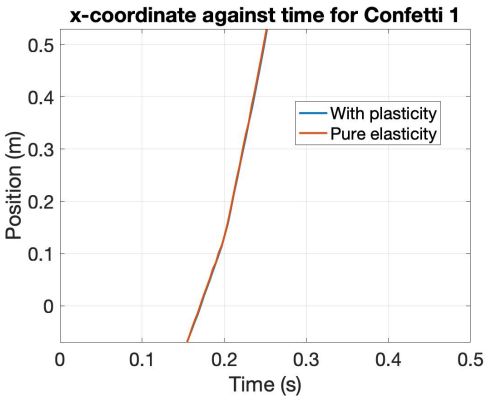

(a) x-coordinate against time, Confetti 1

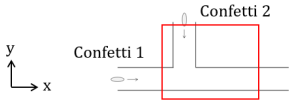

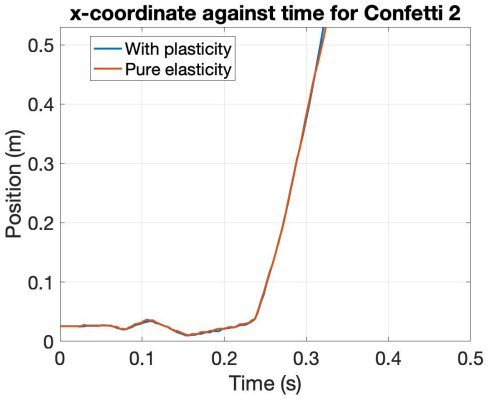

(b) x-coordinate against time, Confetti 2

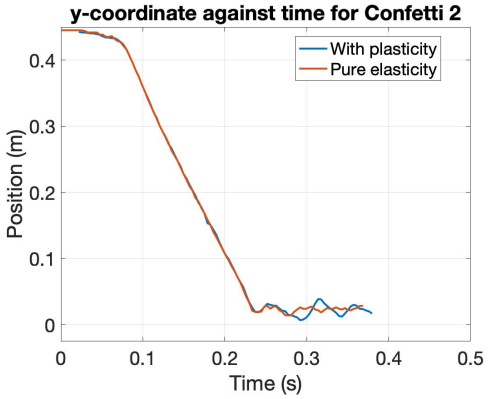

(c) y-coordinate against time, Confetti 2

Figure 6.24: The position against time for the two confetti comparing plasticity and pure elasticity, top view.

The conclusion that can be made after assessing these graphs, is that the plasticity has next to no effect on the position and velocity of the confetti. This coincides well with what is observed in the experiments, where the confetti did not deform considerably. However, this conclusion can only be made for these low flow velocities. For higher velocity flow, an impact with the other confetti or a wall could result in plastic deformation since the confetti would have higher momentum.

6.4 Sources of error

Regarding the numerics, several approximations are made in the FSI-model. Ideal gas is assumed and the k-ϵ model is used for the turbulence, which time averages the flow. The prism layers in the mesh along the walls could be increased, to resolve the boundary layer and near wall effects better. However, this would heavily increase the cell count thus increasing the simulation time even more. An adaptive mesh refinement would be optimal in this case, allowing a fine mesh to surround the confetti while keeping a coarser mesh in the rest of the pipe. Unfortunately, this is a meshing method not yet available for FSI when using STAR-CCM+ and Abaqus/Standard.

There are some deviations in the experiments, due to the human factor. The release time is not the exact same and since the confetti were held and released by hand, the initial

position deviated slightly between runs, which needs to be taken into consideration. Secondly, a PVC pipe was used in the physical experiments to be able to film through it, even though the knife roller is made of steel. This changes the contact conditions between the confetti and the pipe and potential problems with static electricity could arise, such as decelerating the paperboard confetti. As the physical experiments were set up, the air flow velocities were measured at the inlets of the pipe. However, there is an error margin of ± 0.2 m/s in the measurement device used, thus resulting in an error margin for the boundary conditions applied in the simulation model. This corresponds to about 4 % of the inlet velocities chosen, which should not result in drastic changes of the fully developed flow. Furthermore, since the tracking of the centroid of the confetti was performed manually, some margin of error might arise, because the center of mass was not marked on the confetti thus had to be guessed in each frame.

Thirdly, it should be noted that it was intended to run a case with the confetti at +5°, however the simulation crashed, despite heavy under-relaxation. This indicates that the process simulated is sensitive to initial conditions and the ultimate trajectory of the confetti.

Finally, one should keep in mind that a stochastic behavior is modeled in these simulations, which requires a large amount of data to make statistically valid conclusions. In this project, four simulation cases are compared which is too little to make general assumptions about the complete process. These simulations only indicate how the confetti might behave in different situations.

Chapter 7

Conclusions

In summary, it was found that the confetti mainly loses kinetic energy, thus speed, when facing the flow with a small cross-sectional area, especially if it is located near a wall. Colliding with the other confetti or with walls in general, does not affect the final evacuations speed as much as expected, since a collision with a wall or confetti could result in a preferable angle in respect to the bulk flow, thus easier gaining speed. It can be concluded that mainly the orientation of the confetti affects its evacuation speed, while a collision between two confetti does not affect the evacuation time. By increasing the pipe diameter, the risk of the confetti getting stuck in the near wall low velocity flow could be decreased, hence obtaining a more efficient evacuation process.

Secondly, the results show that the initial angle of the confetti affects its initial movement, which in turn can affect the evacuation time. For positive initial inclinations, the confetti has a tendency to move downward increasing the risk of decelerating by the slow near wall flow. However, for negative inclination angles the confetti will move upward, making it easier to be caught by the main flow since gravity prevents the confetti of getting stuck along the upper pipe wall. Thus, for a more efficient evacuation process, the confetti should enter the pipe with a negative inclination angle.

Thirdly, it was observed that the simulations generally over-predict the evacuation speed compared to the physical experiments, indicating that not all losses are captured by the FSI-model. This could be the result of a slight static electrical charge on the PVC pipe, decelerating the paperboard confetti more than a steel pipe would have. It could also be a result of the variation in initial and flow conditions between experiments due to the human factor. To make proper statistically correct conclusions more data is needed, since stochastically random processes are simulated, which are highly dependent on the initial conditions.

Furthermore, it was shown that it is not necessary to include plastic deformation in the material model. One might even consider modeling the confetti as a rigid body in future simulations to save computational time. However, this assumption is only valid for low bulk flow velocities. If the flow velocities were to be increased, larger deformations would be expected, due to higher momentum of the confetti.

Finally, it can be concluded that the simulations capture the trajectory, the behavior of and the interaction between the confetti well, although the confetti velocity is over-predicted. One can say the simulation model is validated and captures the course of event good enough. Since it is numerically stable, the model is suitable for future research and development.

7.1 Future research and development

Now that we have gained some insight on how the confetti behave, interact and deform in the airflow, we are also one step closer to answer the question on why and how the problems during the evacuation process occur. The Final model is numerically stable enough to be suitable for future research and development, such as optimizing the design of the knife roller to obtain an efficient evacuation process.

For further understanding for the FSI-model, a sensitivity analysis of the turbulence model could be performed. This would give a better comprehension of how the turbulence model affects the flow, thus the trajectory and behavior of the confetti in the pipe flow. It would also be interesting to change the wall treatment, by choosing the Low Y+ Wall Treatment instead. For the mesh applied in this model, this could result in a better resolution of the flow properties near the wall, such as the pressure, which might influence how the confetti moves and deforms.

For future development of this model, to finally reproduce what happens inside the knife roller of the converting machines, it would be interesting to expand the geometry further and including more branches to the sides. It would be interesting to see how this would change the flow inside the pipe and thus the trajectory of the confetti.

A second aspect to investigate, would be how the confetti behave if more than two confetti were to be included in the T-junction pipe. In this fashion, the simulations would come closer to reality, while still maintaining a simple domain. However, this would also increase the simulation time considerably. The Modified model took about one day to run and the model with two paper confetti included required three days. Including three or even more confetti, could result in large run times, since every additional co-simulation surface requires more computational resources.

Since the flow velocity within the knife roller is considerably higher than applied in this project, it would be of interest to increase the flow velocity to investigate the changes compared to the results presented here. However, a higher flow velocity would require a smaller time-step to resolve the movement of the flow, thus the confetti, properly. This would in turn result in even higher simulation times. However, one might consider running the model, using the Mesh 2 from the mesh sensitivity analysis. This is about 2 % less accurate but is 50 % faster compared to the current mesh, Mesh 3. This would most definitely yield results close enough to reality, while improving the computational time.

References

[1] T. Richter. *Fluid-structure Interactions - Models, Analysis and Finite Elements*. Springer International Publishing, 2017.

[2] Tetra pak - solutions. `https://www.tetrapak.com/solutions`. Retrieved 2021-01-07.

[3] N. Ottosen and H. Petersson. *Introduction to the finite element method.* Prentice Hall, 1992.

[4] N. Ottosen and M. Ristinmaa. *The mechanics of constitutive modeling*. Elsevier, 2005.

[5] E. Borgqvist, T. Lindström, J. Tryding, M. Wallin, and M. Ristinmaa. Distortional hardening plasticity model for paperboard. *International Journal of Solids and Structures*, 2014.

[6] N. Stenberg. A model for the through-thickness elastic–plastic behaviour of paper. *International Journal of Solids and Structures*, 2003.

[7] Dassault Systèmes, SIMULIA Corp. *Abaqus Analysis User's Manual*, 2016. `http://132.235.17.20:2080/v2016`.

[8] F. White. *Fluid Mechanics, Seventh Edition*. The McGraw-Hill Companies, Inc, 2011.

[9] H. K. Versteeg and W. Malalasekera. *An Introduction to Computational Fluid Dynamics: The Finite Volume Method*. Pearson Education Limited, 2007.

[10] S. Pope. *Turbulent Flows*. Cambridge University Press, 2018.

[11] Siemens Product Lifecycle Management Software Inc. *Simcenter STAR-CCM+ User Guide*, Version 2019.1.

[12] H. Hadžić. *Development and application of a Finite Volume Method for the computation of flows around moving bodies on unstructured, overlapping grids*. PhD thesis, Technischen Universitat Hamburg-Harburg, 2005.

[13] H. J. Bungartz, M. Mehl, and M. Schäfer. *Fluid Structure Interaction II - Modelling, Simulation, Optimization*. Springer-Verlag Berlin Heidelberg, 2010.

[14] A. Quarteroni, L. Formaggia, and A. Veneziani. *Cardiovascular Mathematics: Modeling and simulation of the circulatory system.* Springer-Verlag Italia, Milano, 2009.

[15] D. Jern and A. Leek. Sharp edge cutting through paperboard. Master's thesis, Lunds Tekniska Högskola, 2017.

[16] D. Brown, R Hanson, and W. Christian. *GNU Tracker - Video Analysis and Modeling Tool*, 2020. `https://physlets.org/tracker/`.

Appendix A

Contact analysis

In Fig. A.1-A.5 the results from the contact analysis can be seen: the contour plot of the velocity displaying the contact between the bottom confetti and the pipe wall and a plot displaying the volume average x-position of the two confetti as a function of time.

Fig. A.1 shows the result when $k = 1e6$ is used for the linear pressure-overclosure. The confetti penetrates the wall and the confetti even go through each other. Clearly, this contact condition does not model the contact realistically.

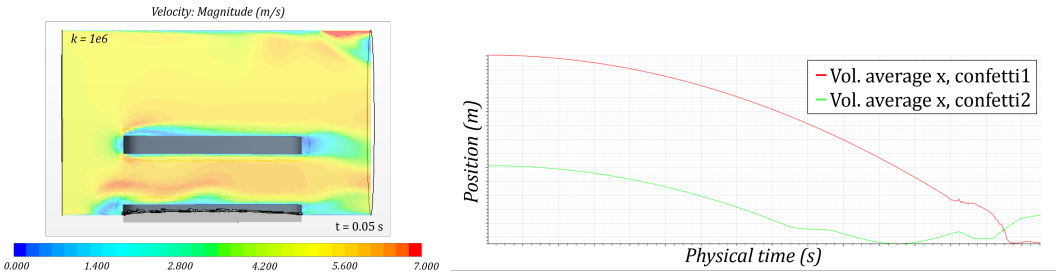

Figure A.1: Contact analysis, pressure-overclosure with 1e6. The plot shows the volume average x-position of the two confetti against time.

In Fig. A.2 and Fig. A.3 the results for $k = 1e8$ and $k = 1e10$ can be seen. Both cases seem to model the contact realistically. The bottom confetti does not penetrate the wall.

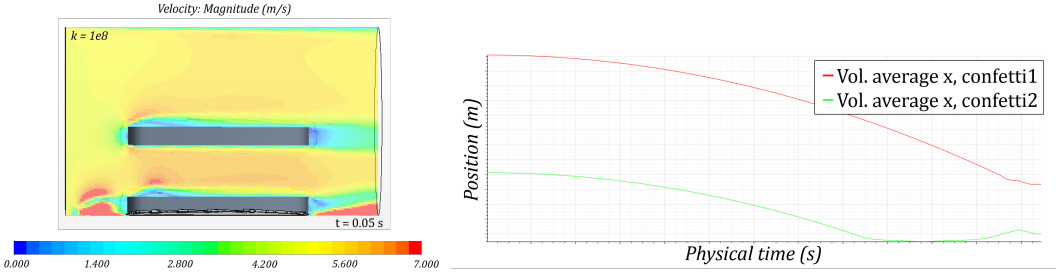

Figure A.2: Contact analysis, pressure-overclosure with 1e8. The plot shows the volume average x-position of the two confetti against time.

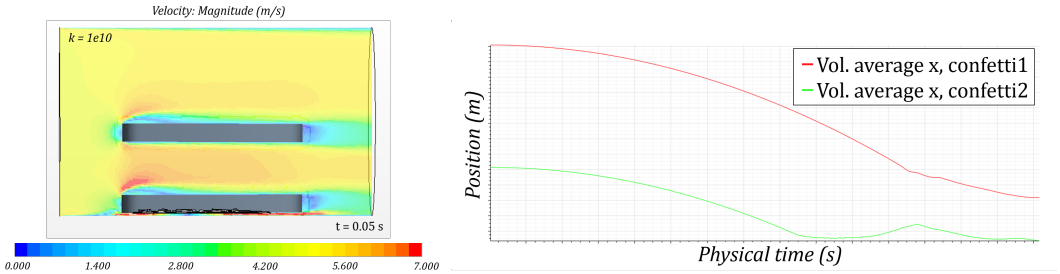

Figure A.3: Contact analysis, pressure-overclosure with 1e10. The plot shows the volume average x-position of the two confetti against time.

The results for the contact condition $k = 1e12$ is to be seen in Fig. A.4. Here the confetti never comes into physical contact with the wall, here we obtain the opposite problem compared to the $k = 1e6$ case.

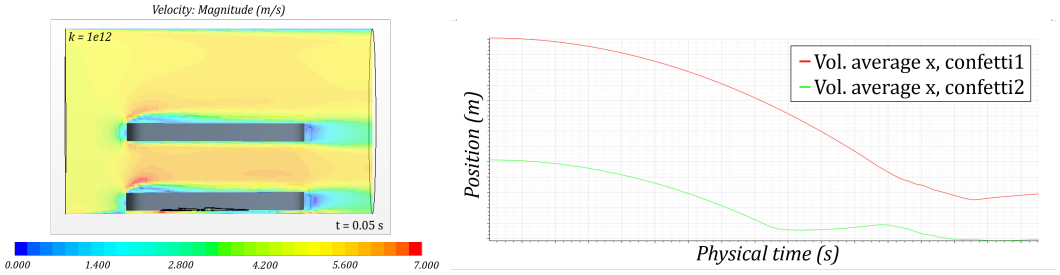

Figure A.4: Contact analysis, pressure-overclosure with 1e12. The plot shows the volume average x-position of the two confetti against time.

The case with an exponential pressure-overclosure, Fig. A.5, models the contact realistically. However, it is not as numerically stable as the linear pressure-overclosure contacts.

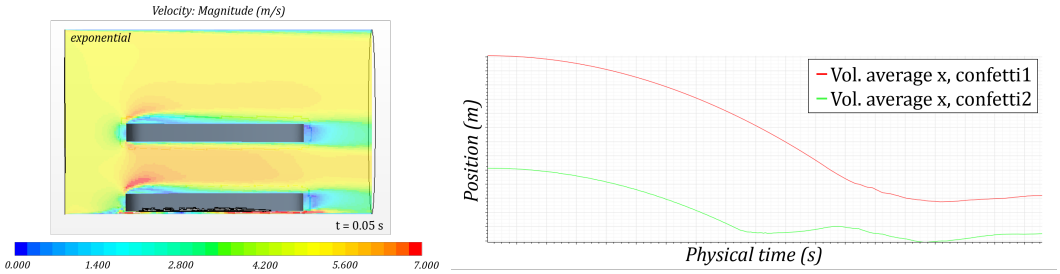

Figure A.5: Contact analysis, exponential pressure-overclosure. The plot shows the volume average x-position of the two confetti against time.

In conclusion, the only contact conditions that model the contact realistically, and is numerically stable, are the ones with a linear pressure-overclosure condition using $k = 1e8$ and $k = 1e10$. Thus, the value in between, $k = 1e9$, is used for the simulations.